

1
2
3
4
5
6
7
8
9
10
11
12
13
14
15
16
17
18
19

**Atg39 selectively captures inner nuclear membrane into luminal vesicles for
delivery to the autophagosome**

Sunandini Chandra*¹, Philip J. Mannino*¹, David J. Thaller*¹, Nicholas R. Ader¹, Megan
C. King, Thomas J. Melia^{1&} and C. Patrick Lusk^{1&}

*These authors contributed equally to this work.
¹Department of Cell Biology, Yale School of Medicine, 295 Congress Ave, New Haven,
CT, 06520

[&]Correspondence to C. Patrick Lusk and Thomas J. Melia
patrick.lusk@yale.edu; thomas.melia@yale.edu

20 **Abstract**

21 Mechanisms that turnover components of the nucleus and inner nuclear membrane
22 (INM) remain to be fully defined. We explore how components of the INM are selected
23 by a cytosolic autophagy apparatus through a transmembrane nuclear envelope-
24 localized cargo adaptor, Atg39. A split-GFP reporter shows that Atg39 localizes to the
25 outer nuclear membrane (ONM) and thus targets the INM across the nuclear envelope
26 lumen. Consistent with this, sequence elements that confer both nuclear envelope
27 localization and a membrane remodeling activity are mapped to the Atg39 luminal
28 domain; these luminal motifs are required for the autophagy-mediated degradation of
29 an integral INM protein. Interestingly, correlative light and electron tomography shows
30 that the overexpression of Atg39 leads to the expansion of the ONM and the enclosure
31 of a network of INM-derived vesicles in the nuclear envelope lumen. Thus, we propose
32 an outside-in model of nucleophagy where INM is delivered into vesicles in the nuclear
33 envelope lumen, which can be targeted by the autophagosome.

34

35

36 **Introduction**

37 The function of the nuclear envelope (NE) is conferred by its biochemical constituents
38 that populate an inner nuclear membrane (INM) with peripherally associated nuclear
39 lamina, an outer nuclear membrane (ONM), and a nuclear pore membrane¹. The latter
40 defines connections between the INM and ONM where embedded nuclear pore
41 complexes (NPCs) control molecular traffic between the nucleus and cytoplasm^{2,3}.
42 Although we have a considerable understanding of the mechanisms that underly
43 molecular exchange through NPCs, it is less well understood how the NE proteome is
44 turned over under either physiological or pathological conditions.

45

46 The need to clear damaged or defective proteins from the nucleus and NE is
47 underscored by the accumulation of nuclear protein aggregates in several human
48 diseases⁴. Further, both NPCs⁵ and the nuclear lamins accumulate damage with age⁶
49 and defects in nuclear transport⁷⁻⁹ and NPC injury may be a cause of certain forms of
50 neurodegeneration including amyotrophic lateral sclerosis¹⁰. Interestingly, the protein
51 constituents of NPCs are also characterized by long half lives in neurons¹¹⁻¹³, which
52 may indicate that they are challenging to productively turnover. Indeed, it is hard to
53 conceptualize how cells might remove these massive macromolecular assemblies
54 without compromising NE integrity. Nonetheless, there is evidence that NPCs may be
55 excised from the NE in both metazoan¹⁴ and in yeast model systems¹⁵⁻¹⁷. While the
56 endosomal sorting complexes required for transport (ESCRT)^{14,16} and the
57 macroautophagy^{16,17} machinery have been implicated in these events, the molecular
58 and morphological steps in these pathways are just beginning to come to light.

59

60 Like NPCs, there is evidence that the lamins can be turned over with several molecular
61 links implicating macroautophagy in this process^{18–21}. Macroautophagy (hereafter called
62 “autophagy”) is a catabolic mechanism that delivers protein aggregates, lipids and parts
63 of (and in some cases, whole) organelles to lysosomes for degradation²². It begins with
64 the formation of a phagophore membrane that is defined by the covalent coupling of the
65 ubiquitin-like protein LC3 (Atg8, in yeast) directly to phosphatidylethanolamine²³. The
66 phagophore expands around the cargo, ultimately sealing the cargo inside a closed
67 double membrane organelle called the autophagosome²⁴. The autophagosome
68 ultimately fuses with lysosomes (or vacuoles, in yeast) where cargo is degraded²⁵.

69

70 Interestingly, there is evidence that LC3 can direct a form of nuclear autophagy
71 (nucleophagy) by binding to Lamin B1 in the context of oncogene activation: this
72 interaction plays a part in the selective clearance of Lamin B1 from the INM¹⁸. However,
73 how a cytosolic phagophore selectively targets the INM or nucleoplasm across the
74 double membraned NE remains unknown. Indeed, in most cases of selective organelle
75 targeting, autophagy cargo adaptors bind to specific proteins and recruit the autophagy
76 machinery to initiate phagophore expansion around themselves^{23,26,27}. While such a
77 nuclear-specific cargo adaptor has not been identified in metazoans, budding yeast
78 have Atg39 (a.k.a. Esm1²⁸), a putative type II transmembrane protein²⁸ that localizes at
79 the NE and is required for the autophagic degradation of both INM and nucleoplasmic
80 proteins^{17,29–33}, but not NPCs¹⁶. Thus, Atg39 is the essential cog in the macroautophagic

81 clearance of INM, but how INM is recognized and delivered to the cytoplasm remains
82 unknown.

83

84 Here, we explore the mechanism of Atg39-mediated nucleophagy in budding yeast. The
85 data support that Atg39 acts from the ONM and connects to the INM through its luminal
86 domain. The luminal domain has functional elements that are required for NE
87 remodeling and the capture of INM cargo into NE-blebs that can be targeted by
88 autophagy. By using correlative light and electron microscopy (CLEM) and tomography
89 and focused ion beam-scanning EM (FIB-SEM) to visualize NE bleb ultrastructure, we
90 observe the capture of INM into vesicles in the NE lumen. We propose a model where
91 nucleophagy proceeds through an outside-in mechanism where putative transluminal
92 interactions coordinate INM and ONM remodeling to ultimately deliver INM cargo to the
93 autophagosome.

94

95 **Results**

96 **Atg39 accumulates at the ONM**

97 Key unknowns to unraveling the nucleophagy mechanism are determining whether
98 Atg39 acts from the ONM or the INM (or both), and whether, like other cargo
99 adaptors^{34–36} it has any inherent membrane remodeling activity. To address the former,
100 we took advantage of a recently developed split-GFP reporter system used to catalogue
101 the INM proteome³⁷. The system exploits a series of mCherry-tagged reporter proteins
102 that are expressed as fusions to GFP¹¹, a 4 kD fragment of GFP, and are localized in
103 the nucleus (GFP¹¹-mCherry-Pus1; Fig. 1a) and ER. The two ER reporters differ in that

104 GFP¹¹ either faces the lumen (mCherry-Scs2_{TM}-GFP¹¹) or the cytosol (GFP¹¹-mCherry-
105 Scs2_{TM}; Fig. 1a). In these backgrounds, the rest of GFP (GFP¹⁻¹⁰) was expressed on
106 either the N- or C-terminus of Atg39 (Fig. 1a) from a galactose-inducible (*GAL1*)
107 promoter; the reconstitution of a fluorescent GFP provides evidence of physical
108 proximity with which to infer localization.

109

110 Taking advantage of the mCherry-Scs2_{TM}-GFP¹¹ ER luminal reporter (Fig. 1a, i), we
111 first confirmed the proposed type II topology^{28,29} of Atg39 as only Atg39-GFP¹⁻¹⁰, but not
112 GFP¹⁻¹⁰-Atg39 resulted in visible GFP fluorescence localized at the NE (Fig. 1b). We
113 also noted that there were NE extensions or “blebs” at sites of reconstituted GFP
114 fluorescence (Fig. 1b, arrows) suggesting that Atg39 expression impacted NE
115 morphology, consistent with prior data²⁸. These blebs were also observed when GFP¹⁻
116 ¹⁰-Atg39 was expressed alongside the cytosolic-facing ER reporter (Fig. 1c, top panels,
117 arrow). Consistent with the conclusion that GFP¹⁻¹⁰-Atg39 is localized specifically to the
118 NE, the ER reporter itself was distributed throughout the NE and ER but the GFP
119 fluorescence was only observed at the nuclear periphery and within the blebs extending
120 from the NE. This was particularly evident when line profiles were drawn that bisected
121 the entire cell and nucleus: only the NE, and not the cortical (c) ER peaks of the
122 mCherry fluorescence (magenta) overlapped with the reconstituted GFP-Atg39
123 fluorescence (green)(Fig. 1d).

124

125 As the ER reporters can access both the ONM and INM (Fig. 1a), we tested whether
126 Atg39 could reach the INM using the nucleoplasmic reporter (Fig. 1a, iii). The

127 extralumenal domain of Atg39 is predicted to be unstructured with a MW of 16 kD.
128 Thus, even with the addition of the GFP¹⁻¹⁰, it should, in principle, be able to pass
129 through the peripheral channels along the pore membrane, which are thought to restrict
130 passage of extralumenal domains larger than ~60 kD^{37,38}. Interestingly, although we
131 observed low levels of GFP fluorescence when GFP¹⁻¹⁰-Atg39 was expressed with the
132 nucleoplasmic reporter (Fig. 1c, bottom panels), this fluorescence was intranuclear and
133 did not accumulate along the nuclear periphery even at low levels of expression (see
134 timecourse of cells treated with galactose, Extended Data Fig. 1a). We interpret these
135 data in a model where Atg39 can cross the pore membrane, but is then liberated from
136 the INM likely through an INM Associated Degradation (INMAD)-type mechanism³⁹⁻⁴².
137 Such a model predicts the existence of a degron sequence in Atg39, likely in its N-
138 terminus. Consistent with this idea, deletion of the N-terminus of Atg39 resulted in the
139 accumulation of a reconstituted nuclear rim fluorescence when GFP¹⁻¹⁰-atg39-(139-
140 398)(Fig. 1a) was expressed with the nucleoplasmic reporter, even after several hours
141 of growth in galactose and thus high levels of expression (Fig. 1e,f, Extended Data Fig.
142 1b), whereas deletion of the C-terminal lumenal (L) domain comprising amino acids
143 169-398 (GFP¹⁻¹⁰-atg39-ΔL)(Fig. 1a) mirrored the full-length protein, albeit with a more
144 visible pool at the nuclear periphery at lower levels (Fig. 1g,h, Extended Data Fig. 1c).
145 Thus, there are sequence elements in the N-terminus of Atg39 that might trigger its
146 removal from the INM. Taken together, the data are most consistent with a model in
147 which Atg39 localizes at the ONM and may in fact be restricted from accumulating at
148 the INM.
149

150 **The Atg39 luminal domain is required for ONM targeting and bleb formation**

151 A model in which Atg39 acts from the outside of the nucleus – in predicts physical
152 interactions that connect Atg39 to the INM through the NE lumen/perinuclear space. To
153 explore this, we generated a deletion series of Atg39 to systematically evaluate the
154 sequence elements that conferred ONM localization; we also evaluated the ability of
155 these constructs to induce NE blebs. As a transluminal interaction is predicted to confer
156 ONM accumulation, we first generated C-terminal deletions that sequentially removed
157 luminal regions that secondary structure prediction suggested were alpha (α) helical in
158 nature (Fig. 2a). Deletion of the terminal two alpha helical segments (GFP-atg39-(1-
159 333)) did not impact NE targeting nor the number of NE blebs observed in each cell
160 (Fig. 2b,e). In contrast, the removal of $\alpha 2$ (GFP-atg39-(1-312)) led to a marked
161 decrease in the number of NE blebs/cell with no obvious impact on NE targeting (Fig.
162 2b,e). These data suggest that the formation of NE blebs requires a discrete sequence
163 motif in the Atg39 luminal domain. They further imply that the NE remodeling observed
164 is not simply an artifact of overexpression but may in fact represent a membrane
165 deforming activity present in the Atg39 luminal domain.

166

167 Removal of $\alpha 1$ abrogated NE accumulation as both GFP-atg39-(1-275) and GFP-atg39-
168 ΔL no longer exclusively accumulated at the NE and were found throughout the cortical
169 ER as well (Fig. 2b). Thus, these data support a model in which the luminal domain of
170 Atg39 has sequence elements required for both NE accumulation ($\alpha 1$) and NE
171 remodeling ($\alpha 2$). In analogy to KASH-proteins that accumulate at the ONM by binding to

172 INM SUN proteins⁴³, we propose that Atg39 accumulates at the ONM by forming a
173 transluminal bridge through direct or indirect interactions with the INM.

174

175 NE targeting and remodeling activities appear to be largely restricted to the luminal
176 domain as N-terminal deletions of Atg39 did not appreciably impact the accumulation of
177 GFP-atg39-(70-398), GFP-atg39-(120-398) or GFP-atg39-(139-398) at the NE, although
178 we did observe more elaborate NE-blebs (Fig. 2c, arrows and Fig. 2e) in these cells that
179 could be correlated to higher levels of these constructs (Extended Data Fig. 2a). This
180 was intriguing as it suggested that interactions with the autophagy machinery, which are
181 mediated through the Atg8 and Atg11-binding motifs²⁹ (Fig. 2a) did not contribute to the
182 formation of the NE-blebs. Consistent with this conclusion, similar numbers of GFP-
183 Atg39 containing NE-blebs were observed in *atg8Δ* and *atg11Δ* strains compared to
184 wild type cells (Fig. 2d,e) with GFP-Atg39 expressed at similar levels in these strains
185 (Extended data Fig. 2b). Thus, the Atg39 luminal domain is necessary for NE targeting
186 and remodeling, which can occur independently of engagement with the core autophagy
187 machinery.

188

189 **The Atg39 luminal domain is required for nucleophagy**

190 The data support a model in which Atg39 can accumulate and mediate NE remodeling
191 from the ONM by virtue of sequence motifs in its luminal domain. To evaluate the
192 importance of these motifs in the nucleophagic clearance of INM proteins, we tested
193 whether they were required for the autophagic degradation of the established integral
194 INM Atg39-cargo, Heh1 (also called Src1)^{29,32} under conditions of nitrogen starvation.

195 We tested the degradation of Heh1-GFP using a standard autophagy assay that relies
196 on the visualization of a stable fragment of GFP (GFP') by Western blot, which is
197 liberated from Heh1-GFP by vacuolar proteases. Consistent with published data²⁹, we
198 observed a ~65% degradation of the total pool of Heh1-GFP in cells grown in medium
199 lacking nitrogen, which was mitigated in the *atg39Δ* strain (Fig. 3a,b). This effect was
200 specific for Heh1-GFP as the relative degradation of Heh1's paralogue, Heh2-GFP, and
201 the nucleoporin Nup82-GFP, were not significantly impacted by *ATG39* deletion (Fig.
202 3c,d).

203

204 To test the role of the Atg39 luminal domain motifs in nucleophagy, we next examined
205 Heh1-GFP degradation in strains expressing luminal truncations from the endogenous
206 *ATG39* chromosomal locus (i.e. under the control of the *ATG39* promoter). Consistent
207 with its importance for executing nucleophagy, the sequential trimming of the C-terminal
208 luminal domain resulted in a reduction of Heh1-GFP degradation that reflected the NE
209 targeting and remodeling analysis (Fig. 2). For example, consistent with the
210 dispensability of the terminal two α -helical segments for NE targeting and remodeling
211 (Fig. 2b,e), the *atg39-(1-333)* allele fully complemented the degradation of Heh1-GFP
212 as the wild type *ATG39* gene (Fig. 3a,b). In contrast, the sequential removal of the α 2
213 (*atg39-1-312*) and α 1 (*atg39-1-275*) coding segments, required for NE remodeling and
214 NE targeting, respectively, resulted in a progressive loss of the ability of these alleles to
215 contribute to Heh1-GFP degradation (Fig. 3a,b). Thus, the luminal sequence motifs that
216 are required for Atg39 NE targeting and blebbing are also needed to effectively execute
217 nucleophagy under conditions of nitrogen starvation.

218 **Atg39-containing NE-blebs are delivered to the vacuole by autophagy**

219

220 Because of the obvious overlap between the requirement of the luminal motifs for NE
221 targeting/remodeling and nucleophagy, we considered the possibility that the NE-blebs
222 formed upon Atg39 overexpression may in fact represent a morphologically relevant
223 intermediate in nucleophagy, albeit exaggerated due to its high levels. Were this to be
224 the case, several criteria needed to be met. First, if the NE-blebs were an intermediate
225 in nucleophagy, they would need to be delivered to the vacuole in a mechanism
226 requiring core autophagy genes. Second, the expectation would be that the NE-blebs
227 would contain cargo specific for Atg39-mediated nucleophagy. Third, the NE
228 ultrastructure driven by Atg39 would need to reflect characteristics of protein-mediated
229 membrane remodeling as opposed to simply membrane expansion or the formation of
230 membrane stacks or lamellae that are common artifacts of the overexpression of NE
231 and ER membrane proteins^{44–52}.

232

233 To address these criteria, we first tested whether the NE-blebs were delivered to
234 vacuoles. To induce autophagy, we treated Atg39-GFP expressing cells with rapamycin
235 while arresting Atg39-GFP production by inhibiting the *GAL1* promoter with the addition
236 of glucose to the medium; delivery of Atg39-GFP to vacuoles (labeled with the FM 4-64
237 dye) was monitored by fluorescence microscopy at 30 min intervals (Fig. 3e). To ensure
238 that Atg39-GFP could be visualized in vacuoles, these experiments were performed in a
239 strain lacking Pep4, a vacuolar protease required for activation of vacuolar hydrolases⁵³.
240 As shown in Fig. 3e, we observed internal vacuolar GFP fluorescence in ~25 % of

241 rapamycin-treated cells beginning at the 60 min time point, which progressively
242 increased to ~95 % by the end of the experiment (150 min; Fig. 3f). Consistent with the
243 idea that Atg39-GFP is progressively being cleared by autophagy, we observed a
244 coincident reduction in Atg39-GFP fluorescence at the nuclear periphery (Fig. 3g).
245 Further, we did not observe GFP fluorescence in the vacuole in carrier-alone (DMSO)
246 treated samples despite some reduction to its levels at the nuclear periphery (Fig.
247 3e,f,g). We interpret the latter to reflect that Atg39-GFP production is inhibited upon
248 addition of glucose to the medium and there is a dilution of Atg39-GFP signal through
249 the ~1.5 cell divisions that occur during the 150 min time course. Therefore,
250 overexpressed Atg39-GFP can be delivered to the vacuole under conditions of
251 autophagy induction by rapamycin treatment.

252

253 To further confirm that overexpressed Atg39-GFP was degraded by autophagy, we also
254 observed the production of GFP' after treating Atg39-GFP expressing cells with
255 rapamycin (Extended Data Fig. 2c). Consistent with the conclusion that this GFP
256 fragment was the product of a vacuolar protease, it was not observed in a *pep4Δ* strain
257 (Extended Data Fig. 2c). Importantly, this autophagy-dependent degradation of Atg39-
258 GFP also required the Atg39 luminal domain as GFP' was not visible upon treatment of
259 *atg39-ΔL*-GFP expressing cells with rapamycin (Extended Data Fig. 2d). Lastly, we
260 confirmed that Atg39-GFP is targeted by autophagy by testing the production of GFP' in
261 both *atg8Δ* and *atg11Δ* strains. Deletion of *ATG8*, and to a lesser extent *ATG11*,
262 abolished its production (Extended Data Fig. 2e). We conclude that Atg39-GFP

263 containing blebs can be delivered and degraded in the vacuole through an autophagy-
264 dependent mechanism.

265

266 **Atg39-derived NE-blebs specifically capture the INM**

267 The second criteria that would provide confidence that the NE-blebs are a potentially
268 physiological intermediate in nucleophagy would be the selective incorporation of Atg39
269 cargo into the blebs. To test this, we monitored the distribution of several integral
270 components of the NE (Fig. 4a) expressed at endogenous levels including NPCs
271 (Nup85), spindle pole bodies (Spc42) and integral INM proteins Heh1 and Heh2, in the
272 context of mCherry-Atg39 expression. Of these, only Heh1 has been shown to be
273 targeted by Atg39-dependent nucleophagy^{29,32}, whereas Nup85 can be degraded by
274 NPC-phagy¹⁷. And indeed, we did not observe any appreciable accumulation of NPCs
275 within the NE-blebs, nor components of the SPB (Fig. 4b, right “GFP” panels, 4c). In
276 striking contrast, Heh1-GFP co-localized with mCherry-Atg39 within at least 50% of the
277 blebs (Fig. 4b, arrowheads, Fig. 4c). As Heh1-GFP is expressed at low levels⁵⁴ often
278 below our threshold for detection even at the NE, we suspected that these numbers
279 were an underestimate. In fact, Heh1-GFP is produced from one of two alternatively
280 spliced forms of the *HEH1-GFP* transcript⁵⁵. By examining the localization of a
281 truncation made before the splice site, a more abundant INM-localized heh1- Δ L-GFP
282 (Fig. 4a) can be visualized in virtually all Atg39-containing NE-blebs (Fig. 4b,c). Further,
283 the brighter heh1- Δ L-GFP allowed the continual monitoring of heh1- Δ L-GFP
284 sequestration into the blebs by timelapse microscopy, which occurs concomitantly with
285 bleb formation (Extended Data Fig. 3, arrowheads).

286

287 Surprisingly, the paralogue of Heh1, Heh2, was not captured with Atg39 in the blebs
288 (Fig. 4b,c) suggesting that there may be some selectivity for subdomains of the INM. To
289 explain this observation, we recently uncovered that a substantial fraction of Heh2 is
290 bound to NPCs⁵⁶, which might prevent Heh2's capture into the NE blebs. To test this
291 idea, we examined the localization of a truncation of Heh2 (heh2- Δ WH; Fig. 4a) that
292 retains INM-targeting information but lacks the ability to bind NPCs, which is conferred
293 by a C-terminal winged-helix (WH) domain⁵⁶. Consistent with the conclusion that binding
294 to NPCs prevents capture of Heh2, heh2- Δ WH-GFP was found in 50% of the visible
295 Atg39-containing NE-blebs (Fig. 4b,c). Thus, taken together, Atg39-dependent NE-
296 blebs can selectively capture the INM over other elements of the NE suggesting that the
297 overexpression of Atg39 might be recapitulating key early steps in an Atg39-dependent
298 nucleophagy pathway.

299

300 **NE-blebs contain a network of INM-derived vesicles in the NE lumen**

301 Lastly, to evaluate whether Atg39 overexpression leads to changes in NE morphology
302 that might illuminate early steps in nucleophagy, we turned to CLEM and tomography.
303 We first examined cells prepared from cultures expressing high levels (Extended Data
304 Fig. 4a) of Atg39-GFP (Fig. 5a, Extended Data Fig. 4b, Supplementary Video 1).
305 Correlation of regions of Atg39-GFP fluorescence (Fig. 5a, Extended Data Fig. 4b,
306 insets) with their position in electron micrographs revealed an impressive proliferation of
307 membranes. These membranes were derived from the NE as direct continuity could be
308 observed with the ONM in single tomographic slices and in 3D reconstructions; ONM

309 ultimately enclosed the entire structure (Fig. 5a, ii, iv-x, arrowheads point to ONM
310 continuity). Most strikingly, captured within the expanded ONM were additional bilayers
311 that are traced in teal (Fig 5a, iv, viii, x), which were most logically derived from the INM.
312 As these membranes were circular within single tomographic slices, we speculated that
313 they were vesicles. Consistent with this, a 3D model of these segmented membranes
314 revealed that they were spherical and similarly sized with a median diameter of ~115
315 nm (Fig. 5a, iii, 5b). Interestingly, a subset of vesicles were connected by membrane
316 constrictions as if undergoing fission (Figure 5a, iii, ix and x, arrows).

317

318 The vesicle diameter measurements were likely an underestimate as it was not possible
319 to capture a large number of entire vesicle volumes within the relatively thin ~200 nm
320 thick tomograms. We therefore also performed FIB-SEM on Atg39-GFP expressing
321 cells. This approach allowed the visualization of 52 whole cell volumes (Extended Data
322 Fig. 5a) revealing cells with expansive networks of NE blebs that emanated from
323 multiple sites on single nuclei (Extended Data Fig. 5b,c, Supplementary Video 2). In
324 these 3D images, we measured the diameter of 982 INM derived vesicles, which had a
325 median diameter of ~164 nm (Fig. 5b). Interestingly, we also observed lipid droplets
326 associated with virtually all of the NE blebs (Extended Data Fig. 5b,c). Thus, the
327 overexpression of Atg39 leads to the generation of a network of likely INM-derived
328 vesicles within the NE lumen alongside an expansion of the ONM with associated lipid
329 droplets. While there are certainly many examples of overexpressed membrane
330 proteins driving changes to membrane morphology, the observed Atg39-dependent
331 morphology is most analogous to those observed in NE egress pathways⁵⁷.

332

333 To gain more insight into the biogenesis of the Atg39-induced compartments, we next
334 performed CLEM on cells expressing lower levels of a GFP-Atg39 fusion (Extended
335 data Fig. 4a). We examined the ultrastructure at NE sites of local GFP-Atg39
336 accumulation and where emerging blebs were visible by fluorescence microscopy (Fig.
337 5c, Extended data Fig. 4c-f). Ultimately, we examined 26 individual Atg39 focal NE
338 accumulations within 23 cells. Of these, 3 could not be attributed to any obvious
339 morphology with 2 being localized at sites where mitochondria were adjacent to the NE
340 (Fig. 5d, Extended data Fig. 4c). In 9 cells, we could unambiguously correlate the
341 fluorescence to either NVJs (3 out of 9) or regions of PMN (6 out of 9)(Fig. 5d, Extended
342 Data Fig. 4d), which may be consistent with recent work supporting a role for Atg39 in
343 PMN³³. And, in a single cell we observed likely extensions to the NE that contained
344 NPCs (Fig. 5d, Extended data Fig. 4e).

345

346 The most prevalent morphology (10 out of 26; Fig. 5d) correlated with GFP-Atg39 is
347 presented in Fig. 5c and Extended Data Fig. 4f. As shown in Fig. 5c, we observed direct
348 continuity between the INM and vesicles within the NE lumen with a ~25 nm constriction
349 or bud neck at the INM. As in the high level expression scenario, these vesicles were
350 again similarly sized (median diameter of 139 nm, Fig. 5b) and were sometimes found
351 in a series where membrane connections could be visualized, segmented and 3D
352 modeled (Fig. 5c panel, iii, iv, Supplementary Video 3). Simultaneously, we observed a
353 clear expansion of the ONM, presumably necessary to accommodate the presence of
354 the extra volume occupied by the vesicles in the NE lumen. Thus, we interpret these

355 structures as precursors to the more elaborate compartments observed upon high level
356 expression of Atg39. These data suggest that Atg39 may have the ability to coordinate
357 membrane remodeling between the INM and ONM and capture components of the INM
358 into vesicles in the NE lumen.

359

360 **Discussion**

361 Atg39 has recently emerged as a key player in the autophagic degradation of nuclear
362 and INM components^{17,29–32,58}, however, how nuclear cargo is selectively packaged and
363 delivered to the cytosolic autophagosome, through the double membraned NE,
364 remained open questions. Here, we provide a framework for answering these questions
365 by proposing an outside-in model of nucleophagy that depends on Atg39 acting from its
366 position at the ONM (see model, Extended Data Fig. 5d). There, Atg39 can engage with
367 the cytosolic autophagy machinery through its cytosolically-exposed N-terminal domain
368 while connecting to the INM through its luminal domain. Evidence in support of this
369 model includes the demonstrated importance of the Atg39 luminal domain not only for
370 NE targeting and NE remodeling (Fig. 2) but also for the nucleophagic degradation of a
371 model Atg39 INM cargo, Heh1-GFP (Fig. 3). Such a mechanism may prove relevant to
372 other forms of nuclear autophagy as well. For example, PMN requires the generation of
373 an ONM-vacuole contact site by the pairing of Nvj1 and Vac8⁵⁹: the close apposition of
374 the INM and ONM at these sites is thought to be mediated by the Nvj1 luminal
375 domain⁶⁰. Interestingly, however, Nvj1 overexpression does not lead to any obvious
376 membrane deformation⁵⁹. Therefore, recent evidence supporting a role for Atg39 in
377 PMN³³ might suggest a model in which Atg39 contributes a membrane remodeling

378 activity capable of co-evaginating the INM and ONM, which is a pre-requisite for both
379 nucleophagy mechanisms.

380

381 Perhaps the most exciting element of this model is the proposal that the INM and
382 associated nuclear content is captured within NE luminal vesicles derived from the INM
383 (Fig. 5; Extended Data Fig. 4,5). Although we acknowledge that these structures are
384 observed upon Atg39 overexpression, we argue that they are likely bona fide early
385 intermediates in a physiological nucleophagy mechanism. Our confidence with this
386 conclusion is based on several data. First, there is the remarkable ability of the Atg39-
387 driven NE-blebs to selectively capture established INM cargo over other components of
388 the NE (Fig. 4). Second, the NE-blebs can be targeted by autophagy provided the
389 signal, yet to be defined, is supplied (Fig. 3e,f). These data also suggest that the
390 interaction between Atg39 and the autophagy apparatus may be regulated in some way,
391 a common theme with selective autophagy cargo adaptors^{61,62}. Third, the
392 overexpression of Atg39 lacking luminal elements, in particular the predicted α helix 2,
393 does not drive analogous morphologies (Fig. 2), further fortifying that they are a specific
394 consequence of Atg39 and not simply an accumulation of an overexpressed integral NE
395 protein.

396 The enclosure of INM within luminal vesicles is also attractive because it provides a
397 harmonious mechanism for how the INM could be selectively removed without
398 impacting NE integrity. The observed ~25 nm membrane necks where the vesicle
399 membranes connect with the INM are strongly suggestive of a protein-scaffold that
400 would maintain their stability and ultimately drive membrane scission. This observation,

401 in addition to the chain-like concatenation of the INM-derived vesicles, strongly
402 resembles morphologies associated with ESCRT function^{63,64}. The hypothesis that
403 ESCRTs may ultimately be involved in a scission event that would liberate the INM-
404 derived vesicle into the lumen is attractive not only because of the many links between
405 autophagy and ESCRTs^{44,65–69}, but also because Heh1, the only well-established INM
406 protein cargo of Atg39²⁹, directly engages with ESCRTs in pathways that ensure NE
407 integrity^{70,71}.

408 Lastly, the removal of INM contents through the proposed mechanism evokes
409 comparisons to the nuclear to cytosolic translocation of so-called “Mega” RNPs in some
410 *Drosophila* neurons that proceeds through a vesicular intermediate in the NE lumen⁷².
411 Thus, we anticipate that the removal of intranuclear contents through the NE lumen will
412 prove to be a generalizable principle of protein, and perhaps RNA, quality control, that
413 will be relevant beyond the yeast system and has in fact already been hypothesized⁷³.
414 Ultimately understanding whether this is the case will require the identification of a
415 mammalian functional homologue to Atg39, which so far remains elusive but is the
416 focus of active investigation.

417

418

419 **Acknowledgements**

420 We thank members of the Melia and LusKing labs for discussion and feedback. We are
421 indebted to Morven Graham, Xinran Liu for invaluable EM expertise. We thank M.P.
422 Rout and S.L. Jaspersen for reagents. This work was funded by grants from the NIH
423 (R21 AG058033 to C.P.L. and T.J.M.; R01 GM105672 to C.P.L.; F32 GM139285 to
424 N.R.A.).

425

426 **Author Contributions**

427 Conceptualization: S.C., P.J.M., D.J.T., T.J.M., C.P.L.; Methodology: S.C., P.J.M.,
428 D.J.T., N.R.A.; Investigation: S.C., P.J.M., D.J.T., N.R.A.; Validation: S.C., P.J.M.,
429 D.J.T., N.R.A.; Formal analysis: S.C., P.J.M., D.J.T., N.R.A.; Writing – original draft:
430 S.C., P.J.M., D.J.T., T.J.M., C.P.L.; Writing – review & editing: All authors; Supervision:
431 M.C.K., T.J.M., C.P.L.;

432

433 **Competing interests**

434 The authors declare no competing interests.

435

436 **Figure legends**

437 **Fig. 1 - Atg39 accumulates at the ONM.**

438 **a**, Schematic of localization and topology of split-GFP constructs. The GFP¹¹-mCherry
439 reporter fusion proteins (i, ii, iii) are constructed as shown in key with localization
440 diagrammed. INM and ONM are inner and outer nuclear membrane, respectively. At
441 bottom are schematics of the Atg39 GFP¹⁻¹⁰ fusions and truncations lacking N or C-
442 termini. The Atg39 transmembrane (TM) domain is depicted as a grey oval. Numbers
443 indicate amino acids.

444 **b**, Deconvolved fluorescence micrographs of cells expressing indicated Atg39 fusion
445 proteins and mCherry-reporters (see inset). GFP, mCherry and merged images shown.
446 Arrowhead points to NE bleb. Scale bar is 5 μ m.

447 **c**, Deconvolved fluorescence micrographs of cells expressing GFP¹⁻¹⁰-Atg39 and
448 indicated mCherry-reporter (inset). GFP, mCherry and merged images shown. Scale
449 bar is 5 μ m. Asterisks indicate vacuolar autofluorescence.

450 **d**, Normalized line profiles of GFP (green) and mCherry (magenta) fluorescence (in
451 arbitrary units, a.u.) bisecting cells as indicated by dotted lines in corresponding top and
452 bottom merge panels from **c**. Position of NE (nuclear envelope) and cER (cortical ER) is
453 indicated by dotted lines.

454 **e**, As in **c**, but with cells expressing GFP¹⁻¹⁰-atg39-(139-398).

455 **f**, As in **d**, but with cells from **e**.

456 **g**, As in **c**, but with cells expressing GFP¹⁻¹⁰-atg39- Δ L. Asterisks indicate vacuolar
457 autofluorescence.

458 **h**, As in **d**, but with cells from **g**.

459

460 **Fig. 2 - The Atg39 luminal domain is required for NE targeting and bleb**

461 **formation.**

462 **a**, Schematic of Atg39 with AIM (Atg8 interacting motif, light orange), Atg11-binding
463 region (blue), predicted transmembrane (TM) helix (grey) and predicted alpha (α)
464 helices 1-4 (colored ovals). Numbers are amino acids.

465 **b**, Deconvolved fluorescence micrographs of the indicated GFP fusion constructs.

466 Numbers indicate amino acid position from **a**. Scale bar is 5 μ m.

467 **c**, As in **b**.

468 **d**, Deconvolved fluorescence micrographs of GFP-Atg39 in the indicated strains. Scale
469 bar is 5 μ m.

470 **e**, Bar chart plotting the quantification of the number of NE blebs per cell in the indicated
471 strains from micrographs in **b-d**. At least 50 cells of each genotype were quantified from
472 three independent experiments. Average and SD are shown. Statistics are from one-
473 way ANOVA where *ns* is $p > 0.05$, and **** $p \leq 0.0001$.

474

475 **Fig. 3 - Atg39-containing NE-blebs are delivered to vacuoles by autophagy.**

476 **a**, The autophagic degradation of Heh1-GFP requires the Atg39 luminal domain.

477 Western blot of proteins (anti-GFP.1) from whole cell extracts derived from cells
478 expressing Heh1-GFP in strains with the indicated *atg39* alleles treated with rapamycin.

479 GFP' is a stable fragment of GFP in vacuoles. Position of molecular weight standards

480 (in kD) at right. To assess relative protein loading, a portion of the blot is shown stained

481 with Ponceau.

482 **b**, Plot of mean and SD of the percentage degradation of Heh1-GFP from three
483 independent experiments as in **a**, Statistics from one-way ANOVA test and Tukey's
484 correction where *ns* is $p > 0.05$, and **** $p \leq 0.0001$.

485 **c**, As in **a** but examining autophagic degradation of Heh2-GFP and Nup82-GFP.

486 **d**, As in **b** but plotting the percentage degradation of Heh2-GFP and Nup82-GFP.

487 **e**, Deconvolved fluorescence micrographs of a timecourse (30 min intervals) of
488 rapamycin or carrier-alone treated (DMSO) cells expressing Atg39-GFP (green) in a
489 *pep4Δ* strain; vacuoles are stained with FM 4-64 (magenta). Merged fluorescent images
490 shown. Scale bar is 3 μm .

491 **f**, Line plot of percentage of cells where Atg39-GFP is visible in vacuoles after treatment
492 with rapamycin (circles and magenta line) or carrier (squares and blue line) over the
493 timepoints indicated. 75 cells were evaluated each from three independent replicates.
494 SD from the mean percentage is indicated by the shaded area.

495 **g**, Violin plot of the fluorescence intensity of Atg39-GFP along the nuclear periphery
496 normalized to background fluorescence in the presence of rapamycin (+) or carrier (-) at
497 the indicated timepoints. 30 cells each from three independent replicates were
498 evaluated, each replicate was normalized to the mean NE fluorescence at 0 min. Solid
499 line denotes the median, width of the violin plot denotes relative frequency of data
500 points. Statistics are from Student's t-test with Welches correction where *ns* is $p > 0.05$,
501 ** is $p \leq 0.01$ and **** is $p \leq 0.0001$.

502

503 **Fig. 4 – INM is specifically captured in Atg39-containing NE blebs.**

504 **a**, Cartoon of protein and protein complexes at the NE including a spindle pole body
505 (SPB) and nuclear pore complex (NPC). Boxed region is magnified at bottom to show
506 integral INM proteins and truncation mutants. LEM is LAP2/emerin/MAN1, WH is
507 winged helix (WH). Numbers are amino acids.

508 **b**, Deconvolved fluorescent micrographs of the indicated GFP fusion proteins under
509 conditions where mCherry-Atg39 expression is repressed (+ glucose, OFF; left panels)
510 or induced (+ galactose, ON; right panels). Merged image of mCherry (magenta) and
511 GFP (green) is also shown. Arrowheads point to NE blebs containing mCherry-Atg39
512 and INM proteins. Scale bar is 5 μ m.

513 **c**, Quantification of percentage of cells with Atg39 blebs colocalized with indicated NE
514 proteins. Error bars are SD from three independent replicates of 100 cells per replicate.

515

516 **Fig. 5 – CLEM of Atg39-GFP reveals expanded ONM with INM-derived vesicles in**
517 **the NE lumen.**

518 **a**, (i) Virtual slice of an electron tomogram of cell with “high” expression of Atg39-GFP
519 (fluorescence image overlaying EM in inset). Boxes represent magnified regions shown
520 in the following panels with corresponding colors. (ii) 3D model of continuous ONM with
521 arrowheads pointing to continuities between substructures. (iii) 3D model of likely INM-
522 derived vesicles within the ONM compartment with arrows pointing to constrictions. (iv)
523 Example virtual slice of tomogram with ONM and INM traced in blue and teal,
524 respectively. (v, vi) Two views of 3D model where ONM and INM are segmented. (vii,
525 viii and ix, x) Further magnifications of single tomographic slices (with and without

526 annotation) as defined by surrounding box color with key in (i). Arrowheads point to
527 continuity of ONM and arrows to INM constrictions. Scale bars are 200 nm.

528 **b**, Quantification of the diameter of INM-derived compartments from cells with “high
529 expression (4 cells), “low” expression (10 cells) of Atg39 from electron tomography or
530 “high” expression of Atg39 from FIB-SEM (52 cells). Total number of INM vesicle
531 diameters measured is indicated in the figure. Median and 95% confidence interval are
532 shown.

533 **c**, CLEM of “low” expressed GFP-Atg39. (i) Fluorescence micrograph of GFP-Atg39
534 with boxed region ultrastructure shown in (ii). Arrowhead points to a region of PMN. (ii)
535 Virtual slice from electron tomogram acquired at of region indicated by the box in panel
536 (i). (iii) Annotation of virtual slice from panel (ii) with the ONM in blue, the INM in teal.
537 (iv) 3D surface rendering of annotated structures in panel (iii). Scale bars: (i), 2 μm ; (ii–
538 iv), 50 nm.

539 **d**, Quantification of indicated morphologies/substructures observed from 26 total GFP-
540 Atg39 NE foci.

541

542 **Extended Data Fig. 1 – The split-GFP reconstitution of intranuclear GFP**

543 **fluorescence depends on the N-terminus of Atg39.**

544 **a-c**, Deconvolved fluorescence micrographs of the indicated GFP¹⁻¹⁰-constructs co-
545 expressed with the nucleoplasmic split-GFP reporter (see inset and Fig. 1a). GFP¹⁻¹⁰-
546 constructs are expressed behind a *GAL1* promoter that is induced by growth in
547 galactose for the indicated times (in hours). GFP (green), mCherry (magenta) and
548 merged images shown. Scale bars are 5 μm .

549

550 **Extended Data Fig. 2 – Assessment of total levels of Atg39 fusion proteins.**

551 **a-e**, Western blot of proteins from whole cell extracts derived from cells expressing the
552 indicated GFP-fusions in indicated strains and drug treatments. GFP detected with anti-
553 GFP antibodies (anti-GFP for a, b; anti-GFP.2 for c, e), HRP-conjugated secondary
554 antibodies and ECL. Position of molecular weight standards (in kD) at right. To assess
555 relative protein loading, a portion of the blots are shown stained with Ponceau.

556

557 **Extended Data Fig. 3 – An Integral INM protein is enriched in NE blebs.**

558 **a**, Deconvolved fluorescence micrographs of a timelapse series showing cells
559 expressing Atg39-mCherry (magenta) and *heh1-ΔL*-GFP (green) with merge at the
560 indicated timepoints after addition of 2% galactose to induce Atg39-mCherry
561 expression. White arrowheads indicate position of NE blebs. Scale bar is 5 μm.

562

563 **Extended Data Fig. 4 – NE ultrastructure at sites of Atg39 accumulation.**

564 **a**, Western blot comparing relative levels of Atg39-GFP (“high” expression) and GFP-
565 Atg39 (“low” expression) to endogenous levels of the nucleoporin, Nup82-GFP (~1600
566 copies/cell). GFP detected with anti-GFP.1. Portion of blot stained with Ponceau shows
567 relative protein loads. Bar graph is quantification by densitometry of the anti-GFP signal
568 normalized to Nup82-GFP.

569 **b-f**, CLEM tomograms from cells expressing “low” or “high” levels of Atg39 as indicated.

570 (i) Fluorescence micrograph with arrows pointing to regions of interest similarly

571 annotated in corresponding EM tomogram.(ii) Virtual slice from electron tomogram with

572 the location of fluorescence from (i) indicated by similarly colored arrows. (iii)
573 Magnification of boxed view in (ii). (iv) Annotation of virtual slices from panel (iii) with the
574 ONM in blue, the INM in teal, vacuole in green and mitochondria in orange. Arrow points
575 to continuity of ONM. Asterisks denote nuclear pores. Scale bars are 100 nm.

576

577 **Extended Data Fig. 5. – FIB-SEM of cells expressing Atg39 with model of**
578 **nucleophagy.**

579 **a**, Total volume of FIB-SEM images of cells expressing Atg39-GFP.

580 **b**, Bar chart of the quantification of NE blebs and associated lipid droplets observed in a
581 total of 52 cells captured within the FIB-SEM volume shown in **a**.

582 **c**, (i) Orthogonal view of a block of FIB-SEM images (from **a**) of a single cell with
583 isotropic resolution of 7 x 7 x 7 nm voxels. (ii) surface rendering of NE (blue), lipid
584 droplets (LDs, yellow), mitochondria (magenta), and vacuole (grey); an SEM image of a
585 single Z-plane is also shown. (iii) top-down view of (ii). (iv) side view of surface
586 rendering of just NE and LDs. Arrowheads point to NE blebs. (v) Annotated SEM image
587 of a single z-slice with ONM blue, LD in yellow. (vi) top-down view of NE and LDs with
588 arrows pointing to NE blebs. (vii, viii) Zoom-view and alternate angles of region
589 containing NE blebs and LDs. Scale bars are 200 nm.

590 **d**, A proposed outside-in model of nucleophagy. Atg39 localizes to the ONM and
591 connects (directly or indirectly) to the INM through luminal motifs. Evagination of the
592 INM and selective capture of INM cargo (Heh1) requires Atg39. INM derived vesicles
593 form after an INM scission event. Subsequent ONM scission would also be required to

594 liberate the NE bleb before its capture by the autophagosome through interactions with
595 the N-terminus of Atg39.

596

597 **Supplementary Table 1** – *S. cerevisiae* strains used in this study.

598 **Supplementary Table 2** – Plasmids used in this study.

599 **Supplementary Video 1** - Related to Fig. 5a. “High” expression of Atg39-GFP results in
600 the formation of NE-blebs. Virtual slices from electron tomograph and 3D surface
601 rendering from tracing throughout the tomography with the ONM (blue) and INM (teal)
602 are shown. Scale bar is 100 nm.

603 **Supplementary Video 2** – Related to Extended Data Fig. 5c. Visualization of whole
604 volumes of cells expressing Atg39-GFP by FIB-SEM with 3D surface rendering of
605 membranes. The NE is shown in blue, lipid droplets in yellow, vacuole in grey, and
606 mitochondria in dark pink. Scale bar is 200 nm.

607 **Supplementary Video 3** – Related to Fig. 5d. “Low” expression of GFP-Atg39 leads to
608 formation of INM derived vesicles in the NE lumen. Virtual slices from an electron
609 tomogram and 3D surface rendering from tracing throughout the tomography with the
610 ONM in blue and INM in teal. Direct continuity between the INM and INM-derived
611 vesicle necks are visible. Scale bar is 50 nm.

612

613 **Materials and Methods**

614 ***Yeast strain construction and culturing conditions***

615 All strains used in this study are listed in Supplementary Table 1. Genomic integration of
616 sequences encoding fluorescent reporter genes, replacement of endogenous gene

617 promoters with *GAL1* promoter and gene deletions were generated using a PCR-based
618 homologous recombination approach using the pFA6a plasmid series^{74,75} (as templates.
619
620 Yeast were cultured to mid-log phase in YP (1% Bacto-yeast extract (BD), 2% Bacto-
621 peptone (BD), 0.025% adenine hemi-sulfate (Sigma)) supplemented with 2% raffinose
622 (R; BD), 2% D-galactose (G; Alfa Aesar) 2% D-glucose (D; Sigma). To maintain
623 selection of plasmids, cells were cultured in Synthetic Complete (SC) medium (Sunrise
624 Science) that lacked the indicated amino acids. All experiments were performed at
625 30°C. Standard protocols for transformations, mating, sporulation, and dissection were
626 followed⁷⁶.

627
628 For induction of autophagy using rapamycin, rapamycin (in DMSO; Sigma-Aldrich) or an
629 equivalent volume of DMSO (carrier) was added to mid-log phase cultures to a final
630 concentration of 250 ng/mL. Samples collected at time points indicated in the figures
631 were prepared for imaging or immunoblotting as described below.

632
633 To induce autophagy by nitrogen starvation, mid-log phase cells were pelleted at ~375
634 g, washed twice with Synthetic Defined (SD) lacking nitrogen (SD-N) medium (0.17%
635 Difco Yeast Nitrogen Base without amino acids and ammonium sulfate (BD), and 2%
636 D), resuspended in SD-N, and returned to a shaking incubator at 30°C for the amount of
637 time indicated in figure legends.

638

639 To assess the localization of Atg39-GFP and GFP-Atg39 under the control of the *GAL1*
640 promoter, strains (SCCPL39, SCCPL40, SCCPL80, SCCPL82, SCCPL95, SCCPL131,
641 DTCPL911, PMCPL87, PMCPL112, PMCPL113, PMCPL114, PMCPL115, PMCPL28,
642 PMCPL29, PMCPL390, PMCPL392, PMCPL422, PMCPL424, and PMCPL471) were
643 grown in YPR to mid-log phase. Expression was induced by the addition of 2% G and
644 images were acquired at timepoints indicated in the figures.

645

646 To examine the subcellular localization of Atg39 in the split-GFP assay, strains
647 containing Atg39 split-GFP fusions under the control of the *GAL1* promoter (PMCPL21,
648 PMCPL34, PMCPL35, and PMCPL298) were transformed with plasmids containing
649 split-GFP-mCherry reporters for the nucleoplasm (pSJ1321), ONM/ER (pSJ1568) or
650 lumen (pSJ1602). Cells grown overnight in media lacking leucine were diluted into
651 YPAR. Expression of Atg39 fusions was induced by the addition of 2% G for 4 h or as
652 otherwise indicated in the figure legends.

653

654 To visualize Atg39-GFP within vacuoles upon induction of autophagy, strain SCCPL22
655 was treated with 2% G to induce Atg39 overexpression. In order to visualize the vacuole
656 membrane, 10 ml of culture was transferred to a foil wrapped tube and incubated with
657 FM 4-64 (1 μ M in DMSO, Molecular Probes) for 30 min at 30°C. Cells were then
658 pelleted and resuspended in YPG. Atg39 expression was arrested after 4 h with the
659 addition of 2% D and samples were split. One culture was treated with rapamycin (final
660 concentration, 250 ng/ml, Sigma-Aldrich) to induce autophagy and the other with DMSO
661 (carrier).

662

663 ***Plasmid generation***

664 All plasmids used in this study are listed in Supplementary Table 2.

665 To generate pPM1 (pFA6a-TRP1-GAL1-GFP¹⁻¹⁰), the region encoding GFP¹⁻¹⁰ was
666 PCR amplified (KOD polymerase, EMD Millipore) from pSJ1256 using primers
667 containing the *PacI* and *Ascl* (New England BioLabs) restriction sites. The amplicon was
668 restriction digested with *PacI/Ascl* (New England BioLabs), gel purified (Qiagen) and
669 ligated (T4 ligase, Invitrogen) into gel purified pFA6a-TRP1-GAL1 digested with
670 *PacI/Ascl* (New England BioLabs). Successful subcloning was confirmed by
671 sequencing.

672

673 To generate pFA6a-3xHA-mCherry-natMX6, the 3xHA epitope sequence was PCR-
674 amplified with Q5 DNA polymerase using pFA6a-3xHA-his3MX6 (Longtine et al., 1998)
675 as a template. The PCR product was assembled into pFA6a-GFP-his3MX6 (Longtine et
676 al., 1998) digested with *Sall* and *PacI* (New England BioLabs) using the Gibson
677 Assembly Master Mix (New England BioLabs).

678

679 To generate pSC8, the 5' sequence of the native promoter and amino acids 1-443 of
680 *HEH1* were amplified via PCR (KOD polymerase, EMD Millipore) from genomic DNA
681 using primers encoding the restriction sites *BamHI* and *HindIII*. The subsequent
682 fragment was gel purified (Qiagen) and ligated using T4 ligase (Invitrogen) into pRS415-
683 GFP plasmid linearized with *BamHI*-HF and *HindIII*-HF. The C-terminal region of Heh1
684 was subsequently introduced by annealing oligos encoding *HEH1* amino acids 449-477

685 flanked with restriction sites *HindIII* and *Sall*, followed by ligation using T7 ligase
686 (Invitrogen). The entire fragment GFP-heh1(1-443)-*HindIII*-heh1(449-477) was excised
687 by restriction digest with *BamHI*-HF and *Sall*-HF. This purified fragment was ligated into
688 *pRS405* digested with *BamHI*-HF and *Sall*-HF.

689

690 pSJ1602 (pRS315-NOP1pr-mCherry-SCS2TM-GFP11) was a gift from Sue Jaspersen
691 (Addgene plasmid # 86417; <http://n2t.net/addgene:86417> ; RRID:Addgene_86417).

692 pSJ1321 (pRS315-NOP1pr-GFP11-mCherry-PUS1) was a gift from Sue Jaspersen
693 (Addgene plasmid # 86413; <http://n2t.net/addgene:86413> ; RRID:Addgene_86413).

694 pSJ1568 (pRS315-NOP1pr-GFP11-mCherry-SCS2TM) was a gift from Sue Jaspersen
695 (Addgene plasmid # 86416; <http://n2t.net/addgene:86416> ; RRID:Addgene_86416).

696 pSJ1256 (pFA6a-link-yGFP1-10-CaURA3MX) was a gift from Sue Jaspersen (Addgene
697 plasmid # 86419; <http://n2t.net/addgene:86419> ; RRID:Addgene_86419).

698

699 ***Microscopy***

700 For all live-cell imaging, mid-log phase cells were gently pelleted and washed with SC
701 media contain 2% D and immediately imaged directly on cover glass. All images were
702 acquired on an Applied Precision DeltaVision microscope (GE Healthcare Life
703 Sciences) equipped with a 100x 1.4 NA oil immersion objective (Olympus), solid state
704 illumination, a CoolSnapHQ² CCD camera (Photometrics) or EMCCD (Photometrics).
705 The microscope stage was maintained at 30°C within an environmental chamber.

706

707 ***Image processing and analysis***

708 All presented micrographs were deconvolved using an iterative algorithm in SoftWoRx
709 (6.5.1; Applied Precision, GE Healthcare). Micrographs and immunoblots were analyzed
710 in FIJI/ImageJ⁷⁷. Unprocessed images were used for quantification of fluorescence
711 intensity.

712

713 Line profiles of fluorescence intensity were generated using the Plot Profile function in
714 FIJI/ImageJ⁷⁷. The minimum and maximum measured values from individual fluorescent
715 channels were normalized to 0 and 1, respectively.

716

717 To quantify changes in Atg39-GFP fluorescence intensity at the NE, the integrated
718 density of a region of interest at the nuclear periphery comprising 4-pixels was
719 measured and normalized to mean background fluorescence.

720

721 ***Secondary Structure prediction***

722 The secondary structure of Atg39's luminal domain was predicted by threading the
723 amino acid sequence of Atg39 through Jpred4⁷⁸.

724

725 ***Statistical methods***

726 Graphs were generated using Prism (GraphPad 9.0). Statistical significance tests were
727 used as indicated in figure legends. Significance values were calculated within Prism
728 (GraphPad 9.0) and p-values are indicated on the graph or in figure legends as: *ns*, $p >$
729 0.05 ; * $p \leq 0.05$; ** $p \leq 0.01$; *** $p \leq 0.001$; **** $p \leq 0.0001$. Error bars are described in
730 figure legends.

731

732 ***Correlative light and electron microscopy***

733 Correlative microscopy of resin-embedded cells was performed as previously
734 described⁷⁹. Expression of Atg39 fusion proteins from cells (DTCPL688 (Atg39-GFP)
735 and PMCPL87 (GFP-Atg39)) cultured in YPAR, was induced by the addition of 2% G for
736 3 h. Cells were then collected by centrifugation for 2 min at 350 g. Yeast slurry was
737 transferred to the 200 µm recess of an aluminum platelet (Engineering Office M.
738 Wohlwend) and placed in an HPM100 (Leica Microsystems) for high pressure freezing.
739 Samples were freeze-substituted in 0.1% uranyl acetate in acetone and embedded in
740 Lowicryl HM20 (Polysciences) using the automated temperature control of an EM-AFS2
741 (Leica Microsystems) with manual agitation and solution exchange following the
742 published protocol⁸⁰. Resin was polymerized under UV light, and the resin-embedded
743 cells were cut into 250 nm thick sections using an ultramicrotome (Leica Artos 3D)
744 equipped with a diamond knife (Diatome) and collected on 200 mesh copper grids with
745 carbon support (Ted Pella, Prod. # 01840).

746

747 Fluorescence and brightfield micrographs of resin-embedded sections were acquired as
748 described above. Several Z-sections were acquired every 200 or 250 nm at each grid
749 square of interest, and in-focus planes were selected for CLEM alignment and
750 presentation in figures.

751

752 Grids selected for tomography were post-stained with uranyl acetate and lead citrate. 15
753 nm protein A-coated gold beads (CMC UMC Utrecht) were adhered to the top and

754 bottom surfaces of grids and used as fiducial markers for the alignment and
755 reconstruction of the tilt series. Single (Fig. 5a, Extended Data Fig. 4b-f) or double (Fig.
756 5c) axis tilt series were collected on a FEI TF20 electron microscope operating at 200
757 kV using a high-tilt tomography holder (Fichione Instruments; Model 2020) from
758 approximately -65° to $+65^{\circ}$ with acquisition at 1° intervals. Images were acquired using
759 SerialEM software⁸¹, at a 2 x 2 binned pixel size of 1.242 nm using a 4k x 4k Eagle CCD
760 (FEI) camera with a 150 μm C2 aperture and a 100 μm objective aperture. Subsequent
761 reconstruction and segmentation were completed in IMOD⁸² in an automated fashion⁸³.
762 For all virtual slices presented, a Gaussian filter in IMOD was applied to reduce noise.
763 Alignment of fluorescence and electron microscopy data was completed using the ec-
764 CLEM Plugin⁸⁴ in the ICY imaging suite⁸⁵. Low magnification EM was related to
765 fluorescence and brightfield micrographs by selecting ~6-8 points that corresponded to
766 features visible in both images.

767

768 ***FIB-SEM***

769 For visualization of entire cellular volumes using FIB-SEM, unfixed yeast slurries loaded
770 into 200 μm aluminum hats were frozen using a Leica HMP100 at 2000 psi. The frozen
771 samples were then freeze substituted using a Leica Freeze AFS unit starting at -95°C
772 using 0.1% uranyl acetate in acetone for 50 h to -600°C , then rinsed in 100% acetone
773 and infiltrated over 24 h at -600°C with Lowicryl HM20 resin (Electron Microscopy
774 Science). Samples were placed in gelatin capsules and UV hardened at -450°C for 48
775 h. The blocks were cured for a further few days before the resin block was trimmed to
776 rough area of interest and the surface cleanly cut using a Leica UltraCut UC7. The

777 entire block was carefully removed with a fine blade, and mounted on an aluminum stub
778 using conductive carbon adhesive and silver paint (Electron Microscopy Sciences,
779 Hatfield, PA, U.S.A.), then sputtered coated with approximately 20 nm Pt/Pd (80/20)
780 using Cressington HR equipment (Ted Pella, Inc. Redding CA) to reduce charging
781 effects.

782

783 A dual beam FIB-SEM (Zeiss CrossBeam 550) using a Gallium ion source was used to
784 mill and SE2 secondary electron detector was used to image the samples. SmartSEM
785 (Zeiss, Jenna Germany) was used to set up initial parameters and to find the regions
786 of interest (ROI) by SEM images at 10 kV, 50 μm width and 30 μm height. The actual
787 depth was 30 μm with 7 nm per pixel and 7 nm per slice. A Platinum- protective layer
788 was deposited at the ROI with the FIB (30 kV, 3 nA) to protect the structure and reduce
789 charging. Milling and highlight was done at 30 kV and 50 pA, with a carbon deposit 30
790 kV 3 nA. A course trench milled 30 kv 30 nA followed by fine milling at 30 kV 3 nA and
791 for final acquisition a cuboid the area of interest was milled at 30 kV and 300 pA. After
792 milling each slice an image was taken by detecting backscattered electrons of a primary
793 electron beam (acceleration voltage of 1.5 kV, imaging current of 2nA, and aperture
794 diameter of 100 μm) with a pixel dwell time of 3 μs . Atlas5 (Zeiss) was used for
795 preliminary SEM stack alignment and FIB/SEM image stacks were saved as TIFF and
796 MRC files. The images were imported into Dragonfly software (ORS, Montreal Canada)
797 for further alignment and segmentation. The total volume imaged was 19.25 μm x 35.8
798 μm x 8.9 μm . Segmentation of structures was done in IMOD⁸², approximately every 35
799 nm.

800

801 ***Immunoblotting***

802 For immunoblotting, cells were harvested as previously described⁸⁶. Briefly, $\sim 1.5 \times 10^8$
803 cells were treated with 10% TCA for 1 h on ice and centrifuged at 15,000 g for 10 min at
804 4°C. The pellet was washed with ice-cold acetone, homogenized by sonication
805 (Bioruptor UCD-200) and pelleted by centrifugation. After two cycles of washing and
806 sonication, the pellet was vacuum-dried for 15 min. The dried cell pellet was then
807 mechanically disrupted with 100 μ l glass beads (Sigma) and 100 μ l urea cracking buffer
808 (50 mM Tris-HCl pH 7.5, 8 M Urea, 2% SDS, and 1 mM EDTA), followed by addition of
809 100 μ l protein sample buffer (Tris-HCl pH 6.8, 7 M urea, 10% SDS, 24% glycerol,
810 bromophenol blue, and 10% β -mercaptoethanol).

811

812 To assess autophagy through GFP-fallout experiments, $\sim 1.5 \times 10^8$ cells were harvested
813 and suspended in 0.2 M NaOH containing 0.1 M DTT, incubated on ice for 10 min,
814 followed by the addition of 10% TCA with incubation on ice for 15 min. After
815 centrifugation at 15,000 g for 5 min at 4°C, the pellet was washed with acetone, vacuum
816 dried, and then resuspended in SDS sample buffer (0.1M Tris-HCl pH 7.5, 2% SDS,
817 10% glycerol, 20 mM DTT) for 10 min at 65°C to dissolve the pellet, followed by 95°C
818 for 3 min.

819

820 Proteins from whole cell extracts were resolved on 4-20% SDS-polyacrylamide gels
821 (BioRad, #4561096), followed by transfer of the proteins to 0.2 μ m nitrocellulose
822 membranes (Bio-Rad). The membranes were blocked in 5% non-fat milk in TBST for 1

823 h and immunoblotted with antibodies against GFP (anti-GFP.1, 4°C overnight, Takara
824 Bio Clontech, 632381 or anti-GFP.2, 1 h room temperature, anti-GFP gift from M. Rout,
825 as indicated in figure legends). Blots were incubated with HRP-conjugated secondary
826 antibodies (1 h room temperature; Sigma) and visualized by ECL (Thermo Fisher
827 Scientific) using a VersaDoc Imaging System (Bio-Rad). Relative protein loading was
828 visualized using Ponceau S Solution (Sigma).

829

830 ***Quantification of autophagic turnover***

831 To calculate the relative percent degradation of GFP-fusion proteins, ROIs were drawn
832 around immunoblot bands corresponding to cleaved GFP' bands and GFP fusion
833 proteins in Fiji/ImageJ⁷⁷ and the total fluorescence intensity was measured. Measured
834 values for GFP' were divided by the sum of GFP' and related GFP-fused full-length
835 protein intensities.

836

837

838 **References**

- 839 1. Ungricht, R. & Kutay, U. Mechanisms and functions of nuclear envelope
840 remodelling. *Nat. Rev. Mol. Cell Biol.* **18**, 229–245 (2017).
- 841 2. Wenthe, S. R. & Rout, M. P. The nuclear pore complex and nuclear transport. *Cold*
842 *Spring Harbor perspectives in biology* vol. 2 (2010).
- 843 3. Schmidt, H. B. & Görlich, D. Transport Selectivity of Nuclear Pores, Phase
844 Separation, and Membraneless Organelles. *Trends Biochem. Sci.* **41**, 46–61
845 (2016).
- 846 4. Bitetto, G. & Di Fonzo, A. Nucleo-cytoplasmic transport defects and protein
847 aggregates in neurodegeneration. *Transl. Neurodegener.* **9**, 25 (2020).
- 848 5. D’Angelo, M. A., Raices, M., Panowski, S. H. & Hetzer, M. W. Age-Dependent
849 Deterioration of Nuclear Pore Complexes Causes a Loss of Nuclear Integrity in
850 Postmitotic Cells. *Cell* **136**, 284–295 (2009).
- 851 6. Karoutas, A. & Akhtar, A. Functional mechanisms and abnormalities of the
852 nuclear lamina. *Nat. Cell Biol.* **23**, 116–126 (2021).
- 853 7. Zhang, K. *et al.* The C9orf72 repeat expansion disrupts nucleocytoplasmic
854 transport. *Nature* **525**, 56–61 (2015).
- 855 8. Chou, C.-C. *et al.* TDP-43 pathology disrupts nuclear pore complexes and
856 nucleocytoplasmic transport in ALS/FTD. *Nat. Neurosci.* **21**, 228–239 (2018).
- 857 9. Cunningham, K. M. *et al.* TFEB/Mitf links impaired nuclear import to
858 autophagolysosomal dysfunction in C9-ALS. *Elife* **9**, (2020).
- 859 10. Coyne, A. N. *et al.* G4C2 Repeat RNA Initiates a POM121-Mediated Reduction in
860 Specific Nucleoporins in C9orf72 ALS/FTD. *Neuron* **107**, 1124-1140.e11 (2020).

- 861 11. Savas, J. N., Toyama, B. H., Xu, T., Yates, J. R. & Hetzer, M. W. Extremely long-
862 lived nuclear pore proteins in the rat brain. *Science* **335**, 942 (2012).
- 863 12. Toyama, B. H. *et al.* Identification of long-lived proteins reveals exceptional
864 stability of essential cellular structures. *Cell* **154**, 971–982 (2013).
- 865 13. Ori, A. *et al.* Integrated Transcriptome and Proteome Analyses Reveal Organ-
866 Specific Proteome Deterioration in Old Rats. *Cell Syst.* **1**, 224–37 (2015).
- 867 14. Toyama, B. H. *et al.* Visualization of long-lived proteins reveals age mosaicism
868 within nuclei of postmitotic cells. *J. Cell Biol.* **218**, 433–444 (2019).
- 869 15. Webster, B. M., Colombi, P., Jäger, J. & Lusk, C. P. P. Surveillance of nuclear
870 pore complex assembly by ESCRT-III/Vps4. *Cell* **159**, 388–401 (2014).
- 871 16. Lee, C.-W. *et al.* Selective autophagy degrades nuclear pore complexes. *Nat. Cell*
872 *Biol.* **22**, 159–166 (2020).
- 873 17. Tomioka, Y. *et al.* TORC1 inactivation stimulates autophagy of nucleoporin and
874 nuclear pore complexes. *J. Cell Biol.* **219**, (2020).
- 875 18. Dou, Z. *et al.* Autophagy mediates degradation of nuclear lamina. *Nature* **527**,
876 105–109 (2015).
- 877 19. Lu, X. & Djabali, K. Autophagic Removal of Farnesylated Carboxy-Terminal Lamin
878 Peptides. *Cells* **7**, (2018).
- 879 20. Borroni, A. P. *et al.* Smurf2 regulates stability and the autophagic-lysosomal
880 turnover of lamin A and its disease-associated form progerin. *Aging Cell* **17**,
881 (2018).
- 882 21. Harhour, K. *et al.* MG132-induced progerin clearance is mediated by autophagy
883 activation and splicing regulation. *EMBO Mol. Med.* **9**, 1294–1313 (2017).

- 884 22. Gatica, D., Lahiri, V. & Klionsky, D. J. Cargo recognition and degradation by
885 selective autophagy. *Nat. Cell Biol.* **20**, 233–242 (2018).
- 886 23. Melia, T. J., Lystad, A. H. & Simonsen, A. Autophagosome biogenesis: From
887 membrane growth to closure. *J. Cell Biol.* **219**, (2020).
- 888 24. Nakatogawa, H. Mechanisms governing autophagosome biogenesis. *Nat. Rev.*
889 *Mol. Cell Biol.* **21**, 439–458 (2020).
- 890 25. Reggiori, F. & Ungermann, C. Autophagosome Maturation and Fusion. *J. Mol.*
891 *Biol.* **429**, 486–496 (2017).
- 892 26. Kirkin, V. & Rogov, V. V. A Diversity of Selective Autophagy Receptors
893 Determines the Specificity of the Autophagy Pathway. *Mol. Cell* **76**, 268–285
894 (2019).
- 895 27. Stolz, A., Ernst, A. & Dikic, I. Cargo recognition and trafficking in selective
896 autophagy. *Nat. Cell Biol.* **16**, 495–501 (2014).
- 897 28. Vevea, J. D. *et al.* Role for Lipid Droplet Biogenesis and Microlipophagy in
898 Adaptation to Lipid Imbalance in Yeast. *Dev. Cell* **35**, 584–599 (2015).
- 899 29. Mochida, K. *et al.* Receptor-mediated selective autophagy degrades the
900 endoplasmic reticulum and the nucleus. *Nature* **522**, 359–62 (2015).
- 901 30. Mostofa, M. G. *et al.* CLIP and cohibin separate rDNA from nucleolar proteins
902 destined for degradation by nucleophagy. *J. Cell Biol.* **217**, 2675–2690 (2018).
- 903 31. Rahman, M. A., Mostofa, M. G. & Ushimaru, T. The Nem1/Spo7-Pah1/lipin axis is
904 required for autophagy induction after TORC1 inactivation. *FEBS J.* **285**, 1840–
905 1860 (2018).
- 906 32. Mizuno, T., Muroi, K. & Irie, K. Snf1 AMPK positively regulates ER-phagy via

- 907 expression control of Atg39 autophagy receptor in yeast ER stress response.
908 *PLoS Genet.* **16**, e1009053 (2020).
- 909 33. Otto, F. B. & Thumm, M. Mechanistic dissection of macro- and micronucleophagy.
910 *Autophagy* 1–14 (2020).
- 911 34. Mochida, K. *et al.* Super-assembly of ER-phagy receptor Atg40 induces local ER
912 remodeling at contacts with forming autophagosomal membranes. *Nat. Commun.*
913 **11**, 3306 (2020).
- 914 35. Jiang, X. *et al.* FAM134B oligomerization drives endoplasmic reticulum membrane
915 scission for ER-phagy. *EMBO J.* **39**, e102608 (2020).
- 916 36. Grumati, P. *et al.* Full length RTN3 regulates turnover of tubular endoplasmic
917 reticulum via selective autophagy. *Elife* **6**, (2017).
- 918 37. Smoyer, C. J. *et al.* Analysis of membrane proteins localizing to the inner nuclear
919 envelope in living cells. *J. Cell Biol.* **215**, 575–590 (2016).
- 920 38. Popken, P., Ghavami, A., Onck, P. R., Poolman, B. & Veenhoff, L. M. Size-
921 dependent leak of soluble and membrane proteins through the yeast nuclear pore
922 complex. *Mol. Biol. Cell* **26**, 1386–94 (2015).
- 923 39. Khmelinskii, A. *et al.* Protein quality control at the inner nuclear membrane.
924 *Nature* **516**, 410–3 (2014).
- 925 40. Foresti, O., Rodriguez-Vaello, V., Funaya, C. & Carvalho, P. Quality control of
926 inner nuclear membrane proteins by the Asi complex. *Science* **346**, 751–5 (2014).
- 927 41. Koch, B. A., Jin, H., Tomko, R. J. & Yu, H.-G. The anaphase-promoting complex
928 regulates the degradation of the inner nuclear membrane protein Mps3. *J. Cell*
929 *Biol.* **218**, 839–854 (2019).

- 930 42. Deng, M. & Hochstrasser, M. Spatially regulated ubiquitin ligation by an
931 ER/nuclear membrane ligase. *Nature* **443**, 827–31 (2006).
- 932 43. Sosa, B. A., Kutay, U. & Schwartz, T. U. Structural insights into LINC complexes.
933 *Curr. Opin. Struct. Biol.* **23**, 285–91 (2013).
- 934 44. Schäfer, J. A. *et al.* ESCRT machinery mediates selective microautophagy of
935 endoplasmic reticulum in yeast. *EMBO J.* **39**, e102586 (2020).
- 936 45. Wright, R., Basson, M., D’Ari, L. & Rine, J. Increased amounts of HMG-CoA
937 reductase induce ‘karmellae’: a proliferation of stacked membrane pairs
938 surrounding the yeast nucleus. *J. Cell Biol.* **107**, 101–14 (1988).
- 939 46. King, M. C., Lusk, C. P. & Blobel, G. Karyopherin-mediated import of integral
940 inner nuclear membrane proteins. *Nature* **442**, 1003–7 (2006).
- 941 47. Volkova, E. G., Abramchuk, S. S. & Sheval, E. V. The overexpression of nuclear
942 envelope protein Lap2 β induces endoplasmic reticulum reorganisation via
943 membrane stacking. *Biol. Open* **1**, 802–5 (2012).
- 944 48. Elgersma, Y. *et al.* Overexpression of Pex15p, a phosphorylated peroxisomal
945 integral membrane protein required for peroxisome assembly in *S.cerevisiae*,
946 causes proliferation of the endoplasmic reticulum membrane. *EMBO J.* **16**, 7326–
947 41 (1997).
- 948 49. Koning, A. J., Roberts, C. J. & Wright, R. L. Different subcellular localization of
949 *Saccharomyces cerevisiae* HMG-CoA reductase isozymes at elevated levels
950 corresponds to distinct endoplasmic reticulum membrane proliferations. *Mol. Biol.*
951 *Cell* **7**, 769–89 (1996).
- 952 50. Smith, S. & Blobel, G. Colocalization of vertebrate lamin B and lamin B receptor

- 953 (LBR) in nuclear envelopes and in LBR-induced membrane stacks of the yeast
954 *Saccharomyces cerevisiae*. *Proc. Natl. Acad. Sci. U. S. A.* **91**, 10124–8 (1994).
- 955 51. Yamamoto, A., Masaki, R. & Tashiro, Y. Formation of crystalloid endoplasmic
956 reticulum in COS cells upon overexpression of microsomal aldehyde
957 dehydrogenase by cDNA transfection. *J. Cell Sci.* **109 (Pt 7)**, 1727–38 (1996).
- 958 52. Snapp, E. L. *et al.* Formation of stacked ER cisternae by low affinity protein
959 interactions. *J. Cell Biol.* **163**, 257–69 (2003).
- 960 53. Ammerer, G. *et al.* PEP4 gene of *Saccharomyces cerevisiae* encodes proteinase
961 A, a vacuolar enzyme required for processing of vacuolar precursors. *Mol. Cell.*
962 *Biol.* **6**, 2490–9 (1986).
- 963 54. Nagaraj, N. *et al.* System-wide Perturbation Analysis with Nearly Complete
964 Coverage of the Yeast Proteome by Single-shot Ultra HPLC Runs on a Bench
965 Top Orbitrap. *Mol. Cell. Proteomics* **11**, (2012).
- 966 55. Rodríguez-Navarro, S., Igual, J. C. & Pérez-Ortín, J. E. SRC1: an intron-
967 containing yeast gene involved in sister chromatid segregation. *Yeast* **19**, 43–54
968 (2002).
- 969 56. Borah, S. Thaller, D.J., Hakhverdyan, Z., Rodriguez, E.C., Rout, M.P., King, M.C.,
970 Lusk, C. P. Heh2/Man1 may be an evolutionarily conserved sensor of NPC
971 assembly state. *Pre-print at bioRxiv*
972 <https://www.biorxiv.org/content/10.1101/2020.06.29> (2020).
- 973 57. Fradkin, L. G. & Budnik, V. This bud's for you: mechanisms of cellular
974 nucleocytoplasmic trafficking via nuclear envelope budding. *Curr. Opin. Cell Biol.*
975 **41**, 125–31 (2016).

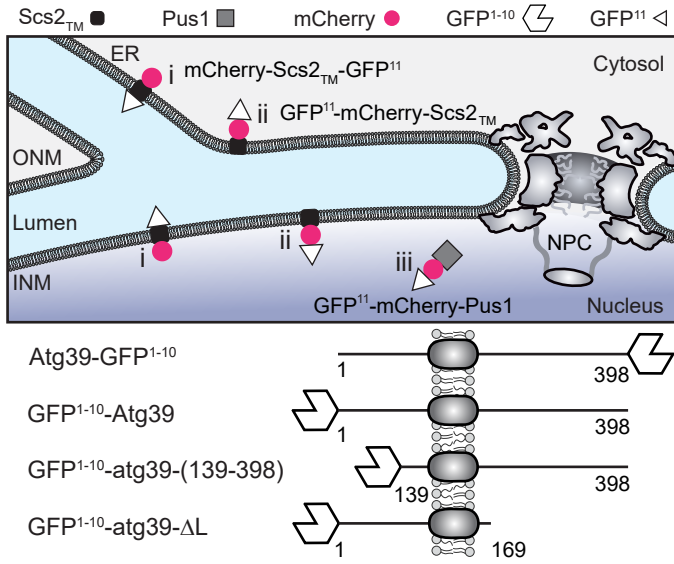
- 976 58. Chen, S. *et al.* Vps13 is required for the packaging of the ER into
977 autophagosomes during ER-phagy. *Proc. Natl. Acad. Sci. U. S. A.* **117**, 18530–
978 18539 (2020).
- 979 59. Pan, X. *et al.* Nucleus-vacuole junctions in *Saccharomyces cerevisiae* are formed
980 through the direct interaction of Vac8p with Nvj1p. *Mol. Biol. Cell* **11**, 2445–2457
981 (2000).
- 982 60. Millen, J. I., Pierson, J., Kvam, E., Olsen, L. J. & Goldfarb, D. S. The luminal N-
983 terminus of yeast Nvj1 is an inner nuclear membrane anchor. *Traffic* **9**, 1653–64
984 (2008).
- 985 61. Farré, J.-C., Burkenroad, A., Burnett, S. F. & Subramani, S. Phosphorylation of
986 mitophagy and pexophagy receptors coordinates their interaction with Atg8 and
987 Atg11. *EMBO Rep.* **14**, 441–9 (2013).
- 988 62. Aoki, Y. *et al.* Phosphorylation of Serine 114 on Atg32 mediates mitophagy. *Mol.*
989 *Biol. Cell* **22**, 3206–17 (2011).
- 990 63. McCullough, J., Frost, A. & Sundquist, W. I. Structures, Functions, and Dynamics
991 of ESCRT-III/Vps4 Membrane Remodeling and Fission Complexes. *Annu. Rev.*
992 *Cell Dev. Biol.* **34**, 85–109 (2018).
- 993 64. Vietri, M., Radulovic, M. & Stenmark, H. The many functions of ESCRTs. *Nat.*
994 *Rev. Mol. Cell Biol.* **21**, 25–42 (2020).
- 995 65. Li, J., Breker, M., Graham, M., Schuldiner, M. & Hochstrasser, M. AMPK
996 regulates ESCRT-dependent microautophagy of proteasomes concomitant with
997 proteasome storage granule assembly during glucose starvation. *PLoS Genet.*
998 **15**, e1008387 (2019).

- 999 66. Zhou, F. *et al.* Rab5-dependent autophagosome closure by ESCRT. *J. Cell Biol.*
1000 **218**, 1908–1927 (2019).
- 1001 67. Loi, M., Raimondi, A., Morone, D. & Molinari, M. ESCRT-III-driven piecemeal
1002 micro-ER-phagy remodels the ER during recovery from ER stress. *Nat. Commun.*
1003 **10**, 5058 (2019).
- 1004 68. Takahashi, Y. *et al.* An autophagy assay reveals the ESCRT-III component
1005 CHMP2A as a regulator of phagophore closure. *Nat. Commun.* **9**, 2855 (2018).
- 1006 69. Zhen, Y. *et al.* ESCRT-mediated phagophore sealing during mitophagy.
1007 *Autophagy* 1–16 (2019) doi:10.1080/15548627.2019.1639301.
- 1008 70. Webster, B. M. *et al.* Chm7 and Heh1 collaborate to link nuclear pore complex
1009 quality control with nuclear envelope sealing. *EMBO J.* **35**, 2447–67 (2016).
- 1010 71. Gu, M. *et al.* LEM2 recruits CHMP7 for ESCRT-mediated nuclear envelope
1011 closure in fission yeast and human cells. *Proc. Natl. Acad. Sci. U. S. A.* **114**,
1012 E2166–E2175 (2017).
- 1013 72. Speese, S. D. *et al.* Nuclear Envelope Budding Enables Large Ribonucleoprotein
1014 Particle Export during Synaptic Wnt Signaling. *Cell* **149**, 832–846 (2012).
- 1015 73. Rose, A. & Schlieker, C. Alternative nuclear transport for cellular protein quality
1016 control. *Trends Cell Biol.* **22**, 509–514 (2012).
- 1017 74. Longtine, M. S. *et al.* Additional modules for versatile and economical PCR-based
1018 gene deletion and modification in *Saccharomyces cerevisiae*. *Yeast* **14**, 953–61
1019 (1998).
- 1020 75. Van Driessche, B., Tafforeau, L., Hentges, P., Carr, A. M. & Vandenhaute, J.
1021 Additional vectors for PCR-based gene tagging in *Saccharomyces cerevisiae* and

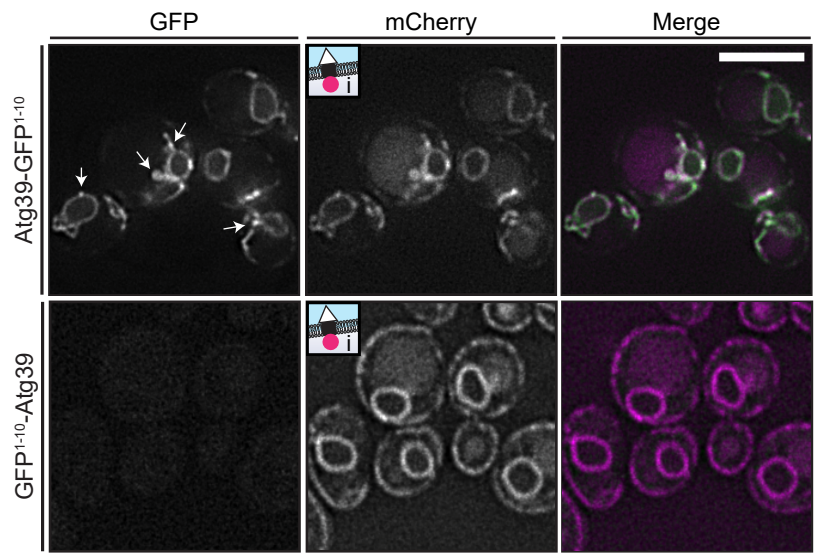
- 1022 Schizosaccharomyces pombe using nourseothricin resistance. *Yeast* **22**, 1061–8
1023 (2005).
- 1024 76. Amberg, D. C., Burke, D. & Strathern, J. N. *Methods in yeast genetics : a Cold*
1025 *Spring Harbor Laboratory course manual. Cold Spring Harbor Laboratory Press*
1026 (Cold Spring Harbor Laboratory Press, 2005).
- 1027 77. Schindelin, J. *et al.* Fiji: an open-source platform for biological-image analysis.
1028 *Nat. Methods* **9**, 676–682 (2012).
- 1029 78. Drozdetskiy, A., Cole, C., Procter, J. & Barton, G. J. JPred4: a protein secondary
1030 structure prediction server. *Nucleic Acids Res.* **43**, W389-94 (2015).
- 1031 79. Kukulski, W. *et al.* Precise, correlated fluorescence microscopy and electron
1032 tomography of lowicryl sections using fluorescent fiducial markers. *Methods Cell*
1033 *Biol.* **111**, 235–57 (2012).
- 1034 80. Kukulski, W. *et al.* Precise, correlated fluorescence microscopy and electron
1035 tomography of lowicryl sections using fluorescent fiducial markers. *Methods Cell*
1036 *Biol.* **111**, 235–57 (2012).
- 1037 81. Mastronarde, D. N. Automated electron microscope tomography using robust
1038 prediction of specimen movements. *J. Struct. Biol.* **152**, 36–51 (2005).
- 1039 82. Kremer, J. R., Mastronarde, D. N. & McIntosh, J. R. Computer visualization of
1040 three-dimensional image data using IMOD. *J. Struct. Biol.* **116**, 71–6 (1996).
- 1041 83. Mastronarde, D. N. & Held, S. R. Automated tilt series alignment and tomographic
1042 reconstruction in IMOD. *J. Struct. Biol.* **197**, 102–113 (2017).
- 1043 84. Paul-Gilloteaux, P. *et al.* eC-CLEM: flexible multidimensional registration software
1044 for correlative microscopies. *Nat. Methods* **14**, 102–103 (2017).

- 1045 85. de Chaumont, F. *et al.* Icy: an open bioimage informatics platform for extended
1046 reproducible research. *Nat. Methods* **9**, 690–6 (2012).
- 1047 86. Zhu, L., Jorgensen, J. R., Li, M., Chuang, Y.-S. & Emr, S. D. ESCRTs function
1048 directly on the lysosome membrane to downregulate ubiquitinated lysosomal
1049 membrane proteins. *Elife* **6**, (2017).
- 1050

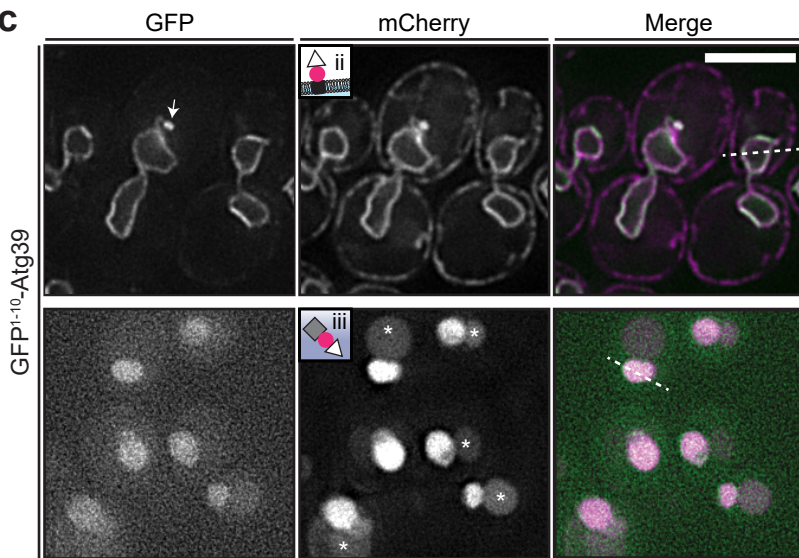
a



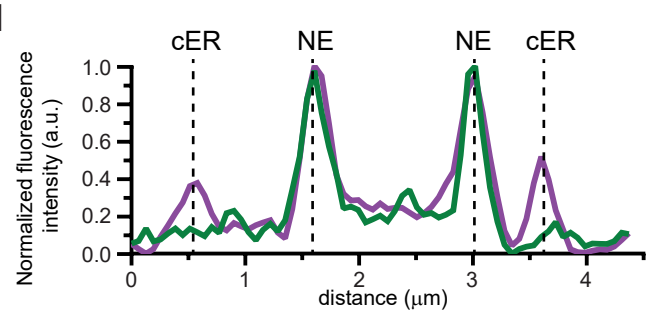
b



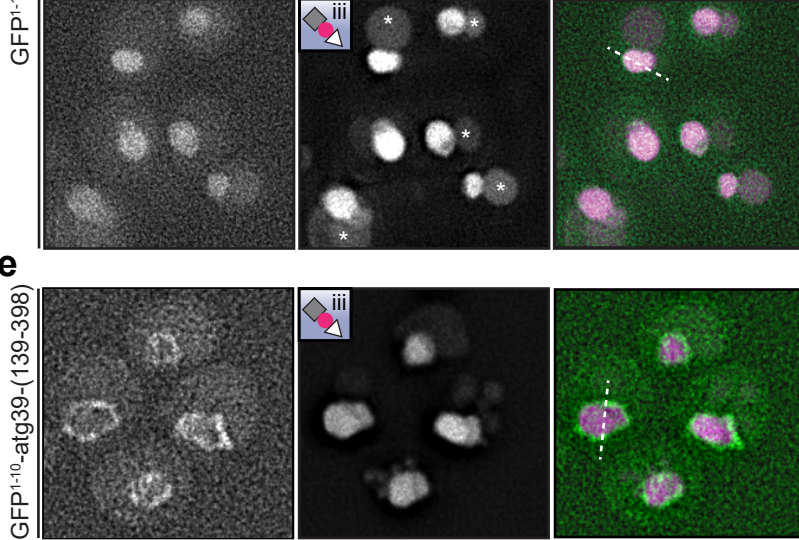
c



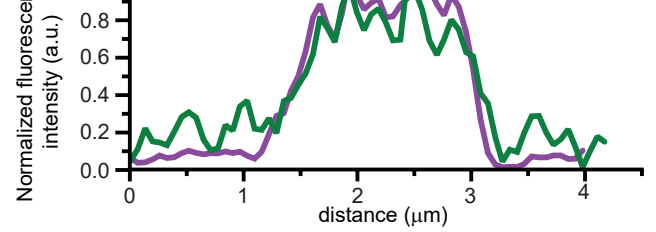
d



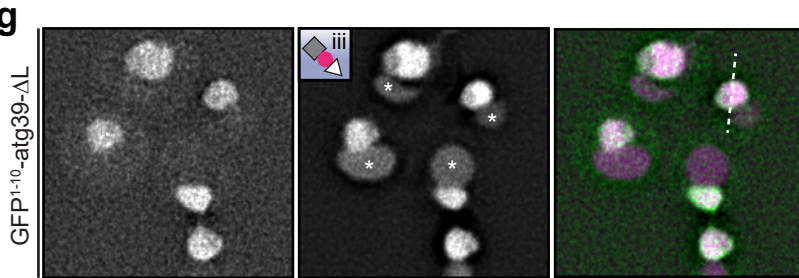
e



f



g



h

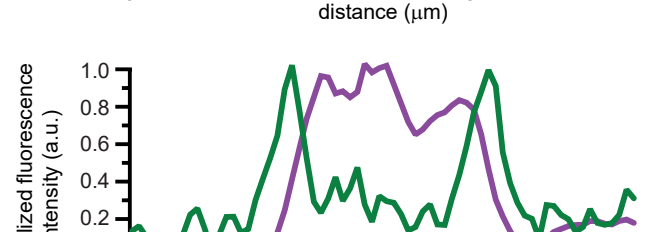


Fig. 2

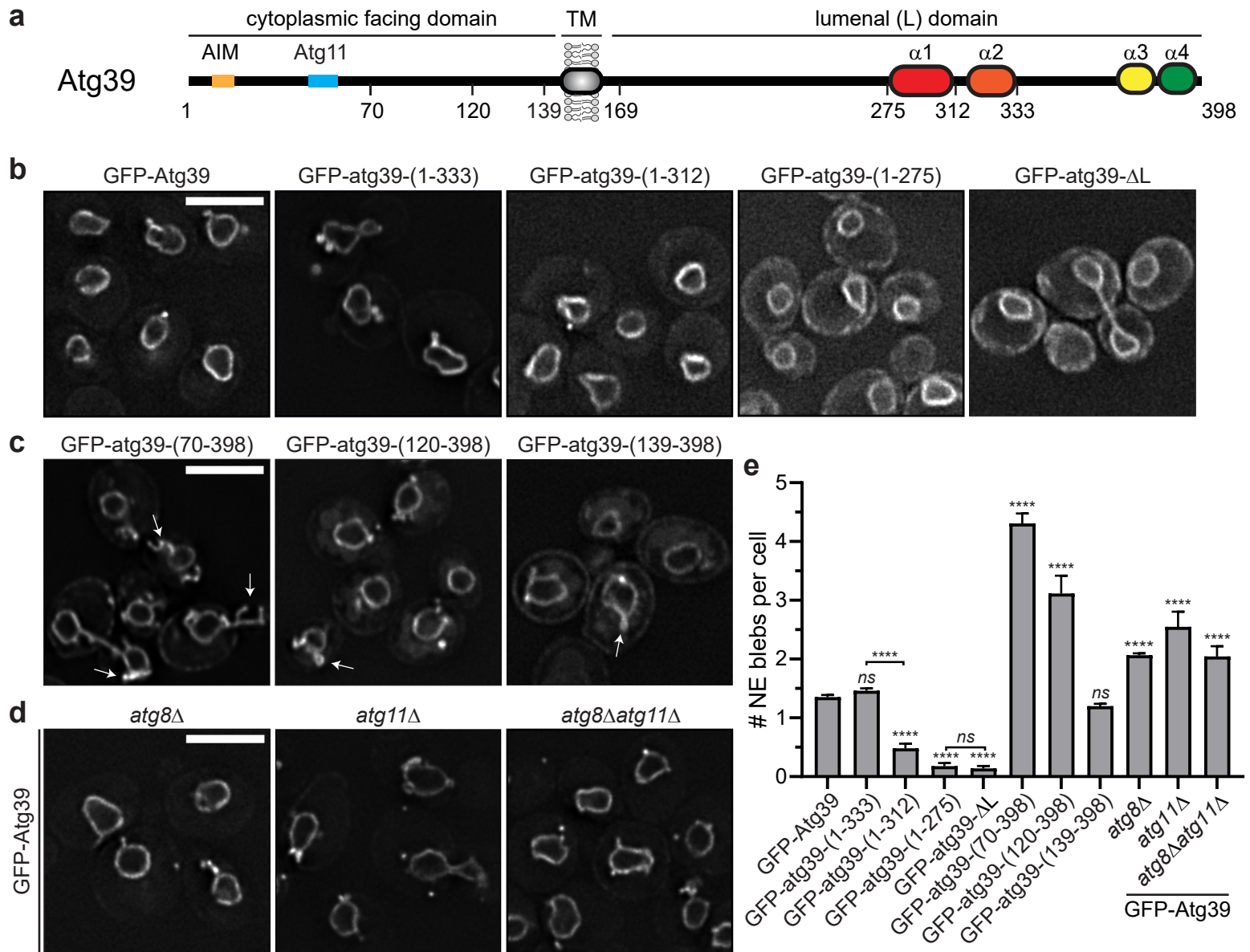
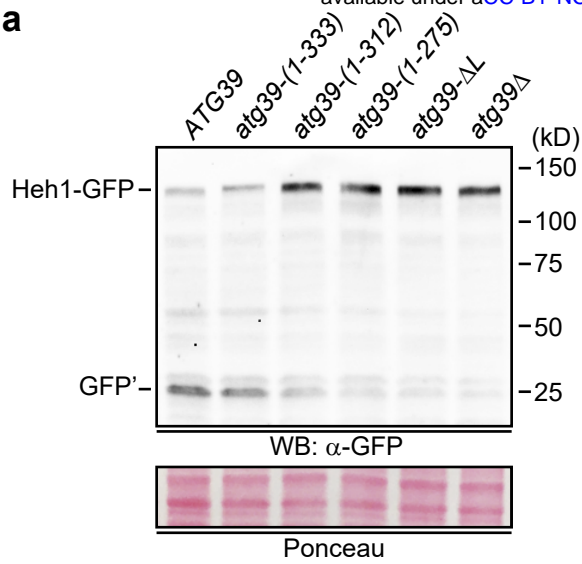
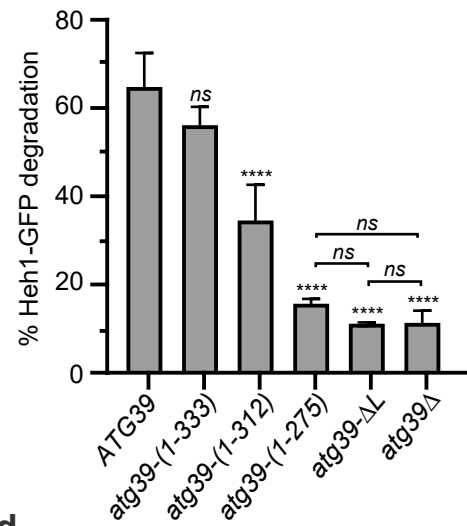


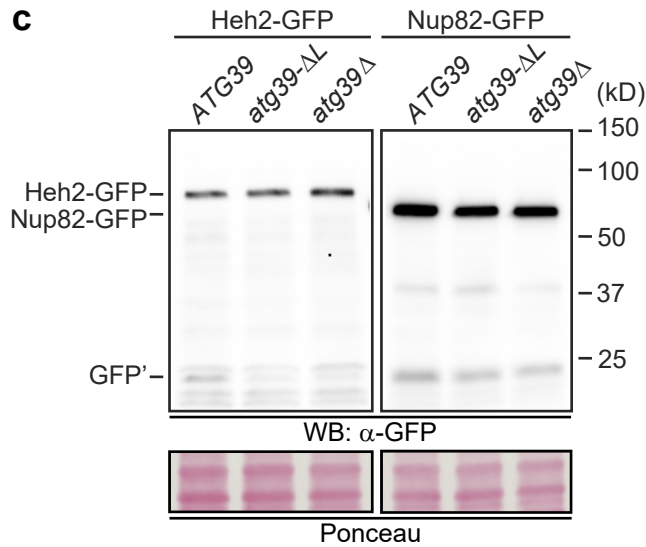
Fig. 3 a



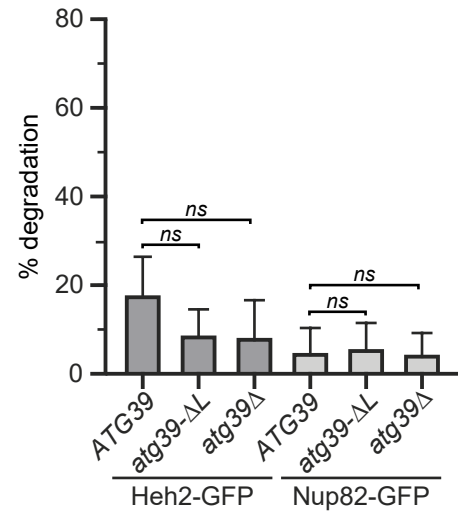
b



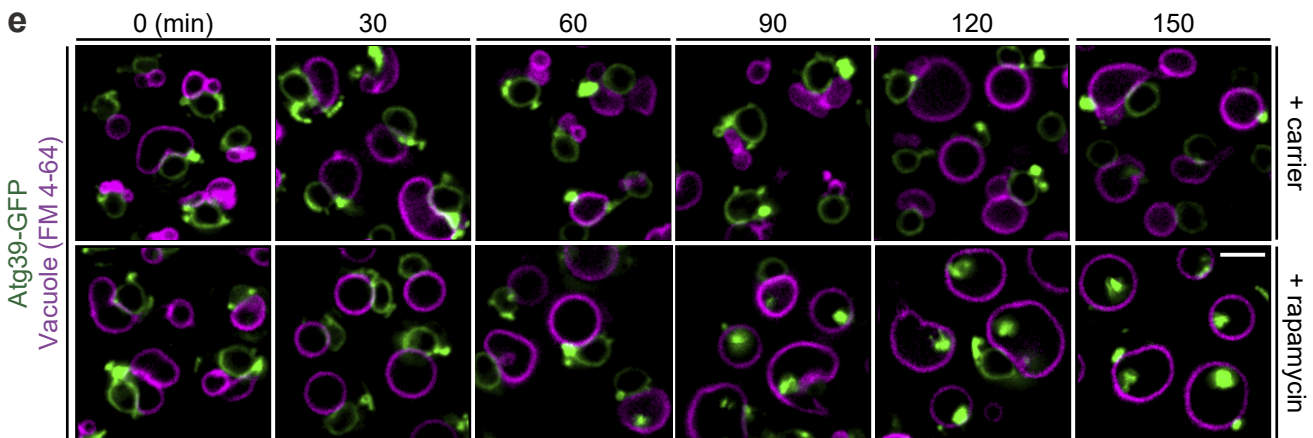
c



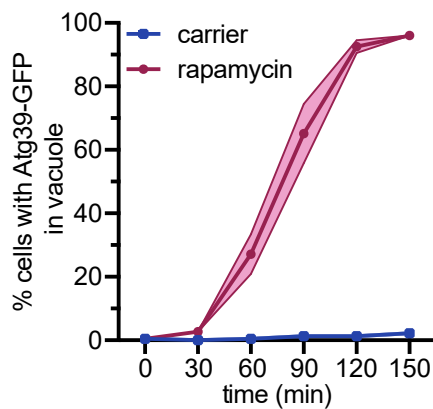
d



e



f



g

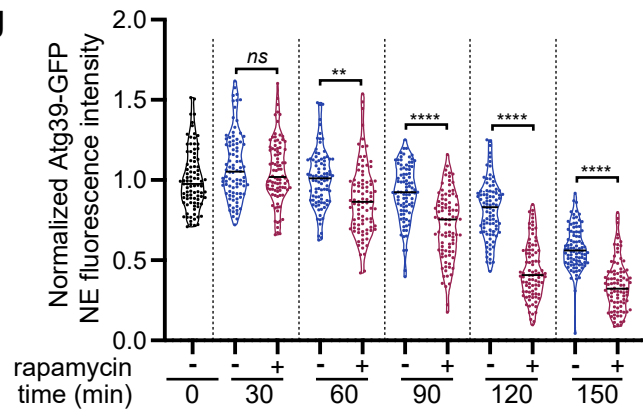
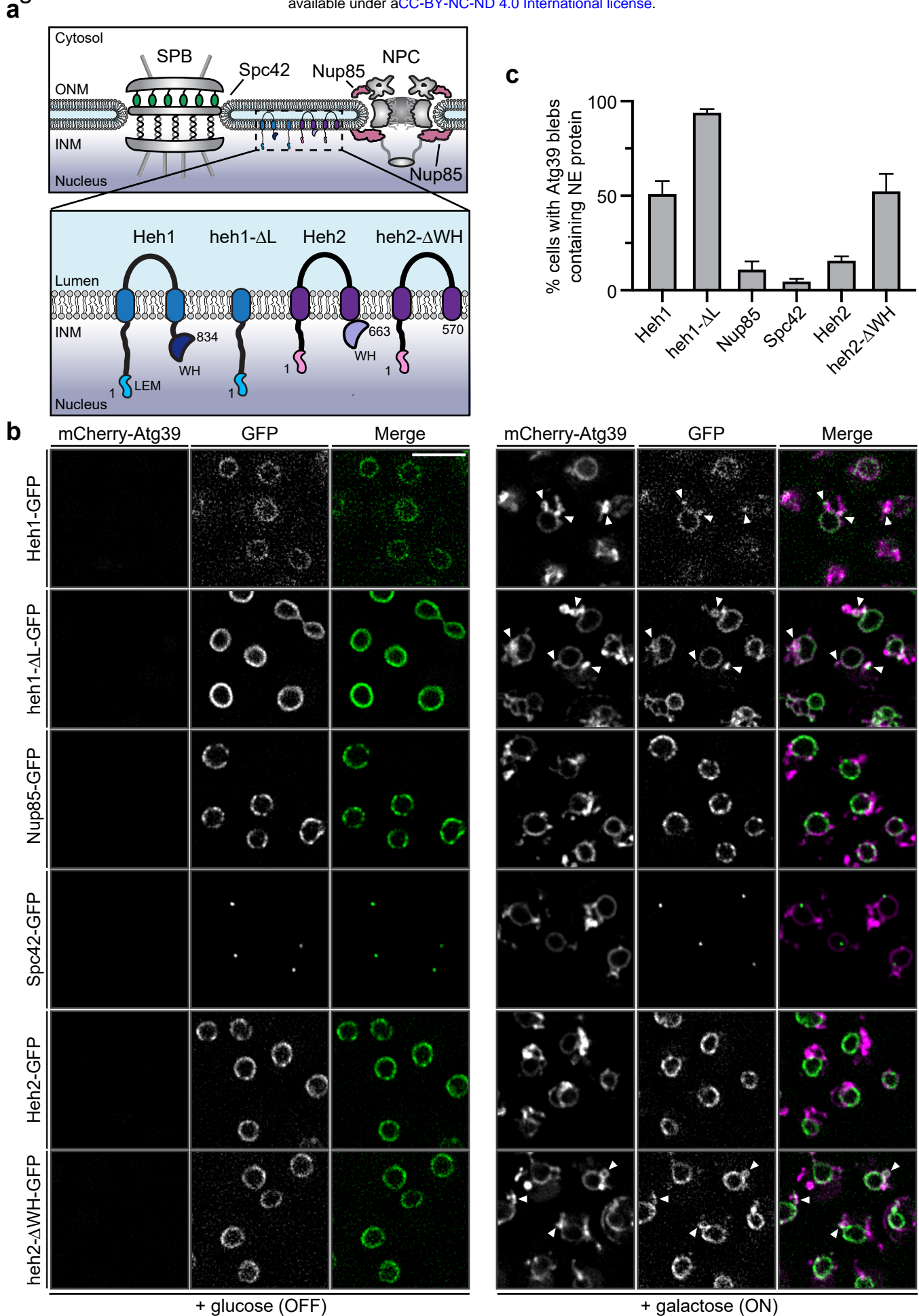
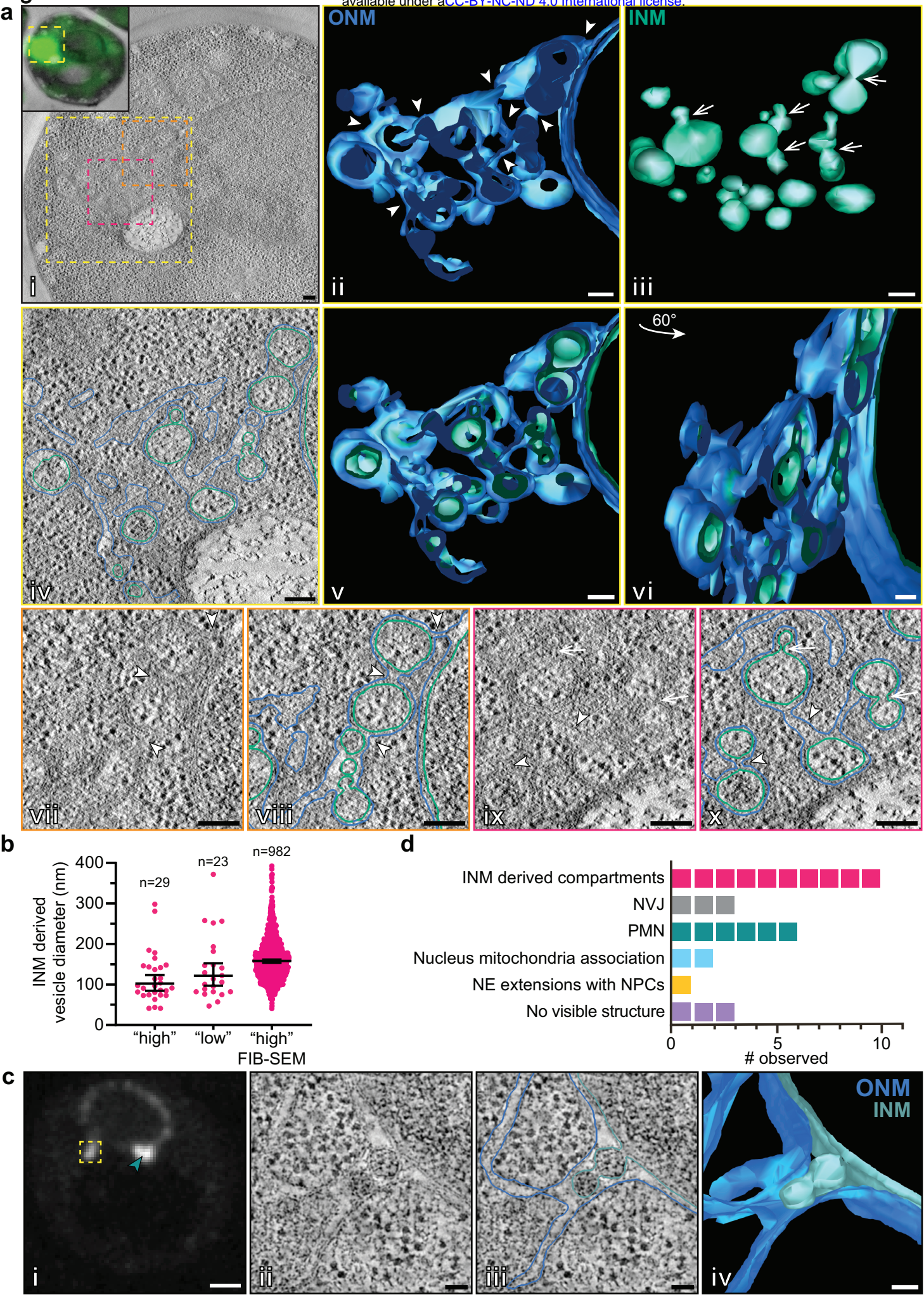


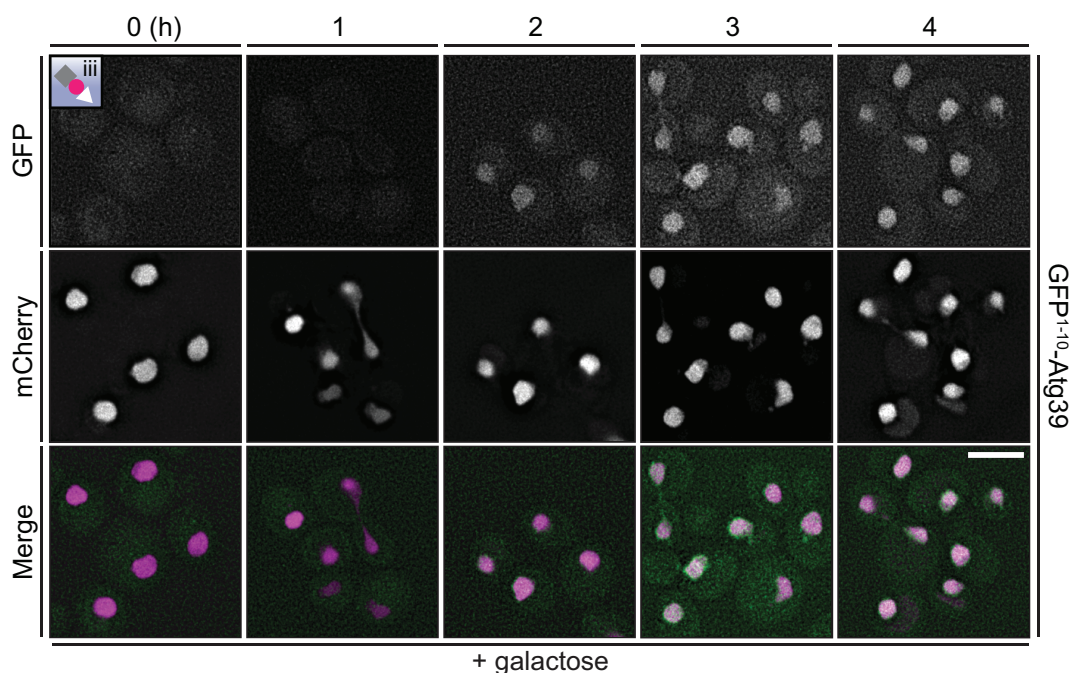
Fig 4





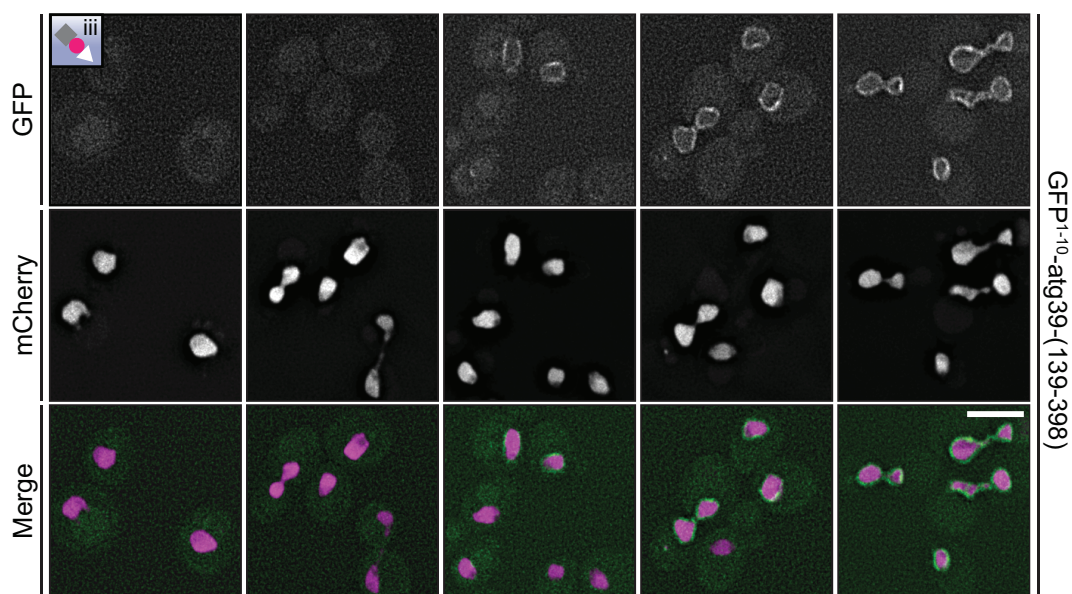
Extended Data Fig. 1

a



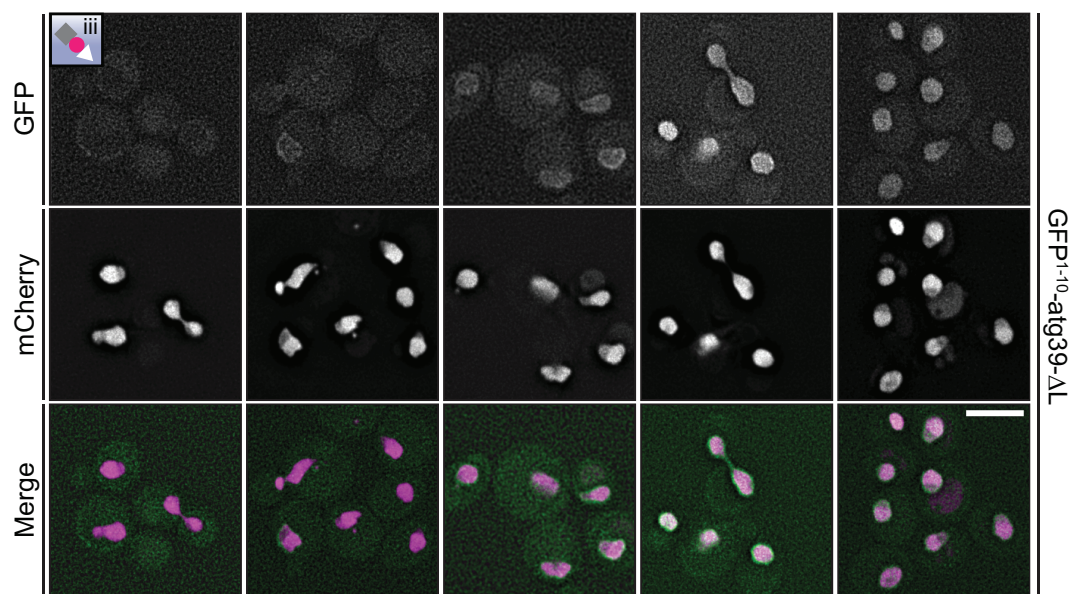
+ galactose

b



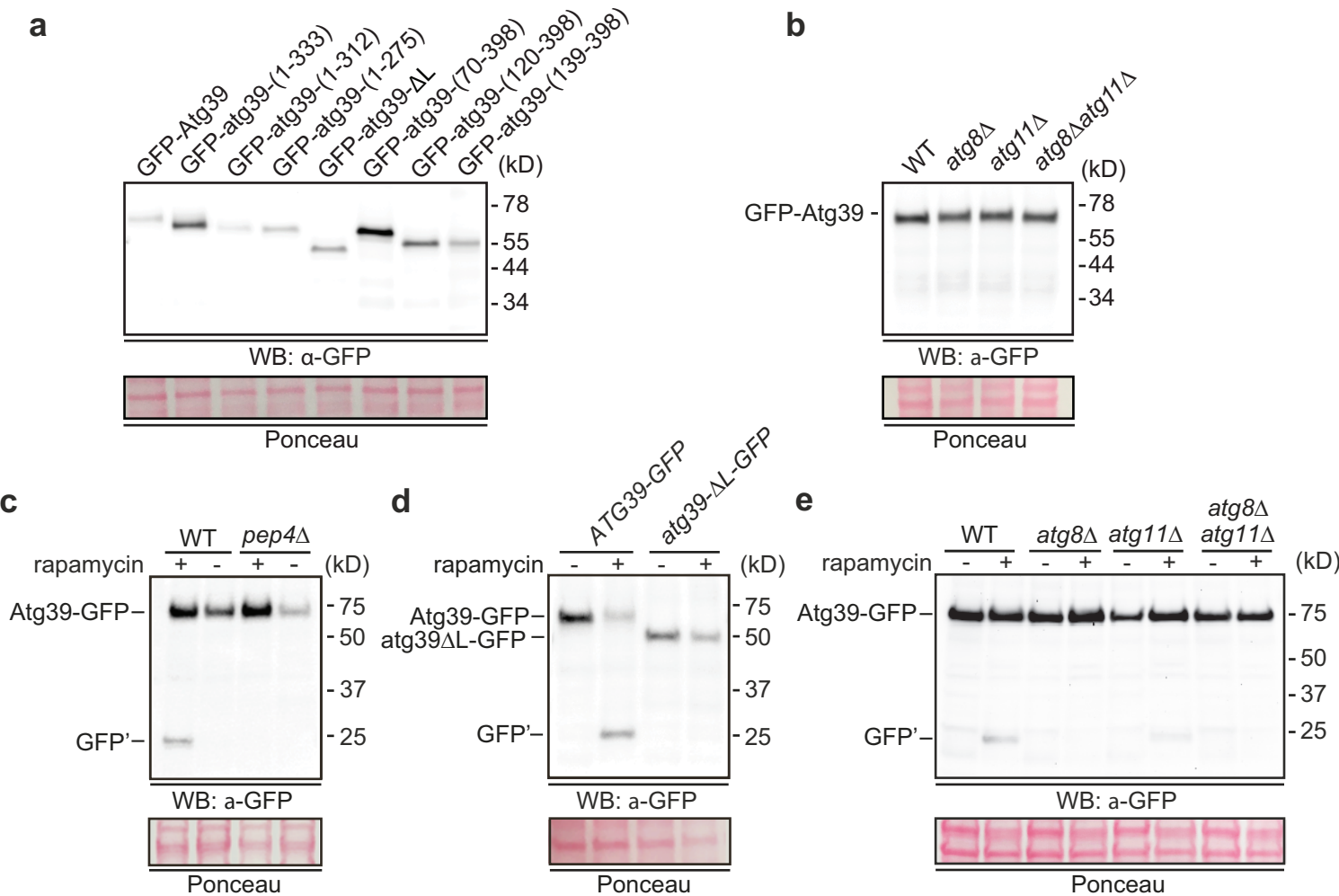
+ galactose

c

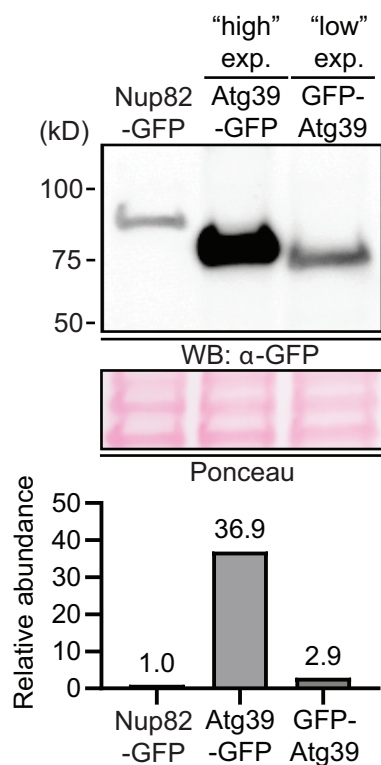


+ galactose

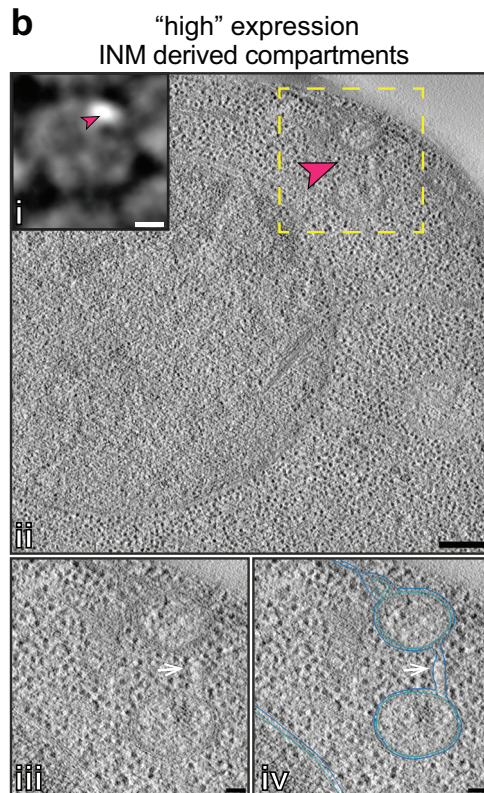
Extended Data Fig. 2



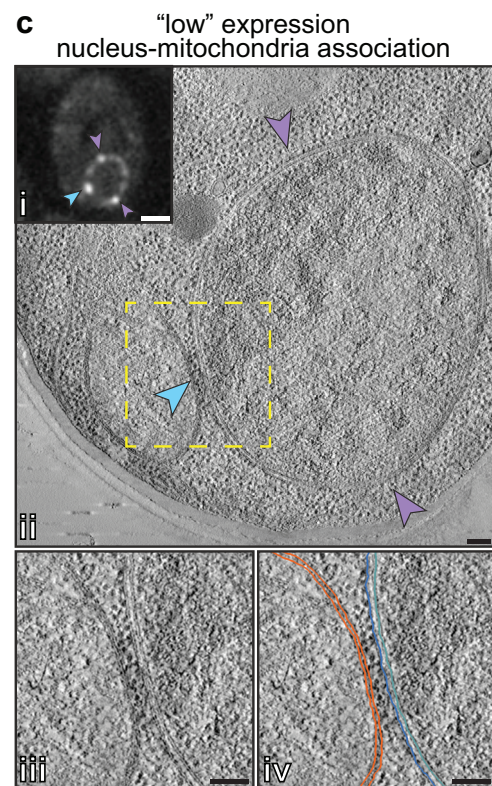
a



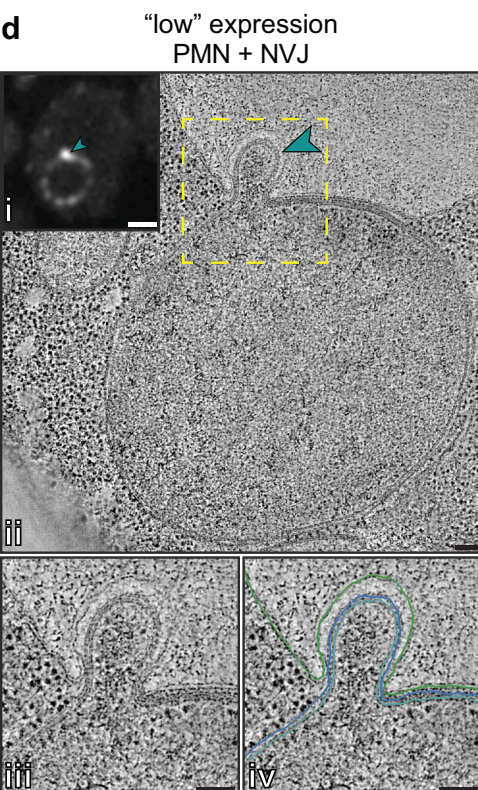
b



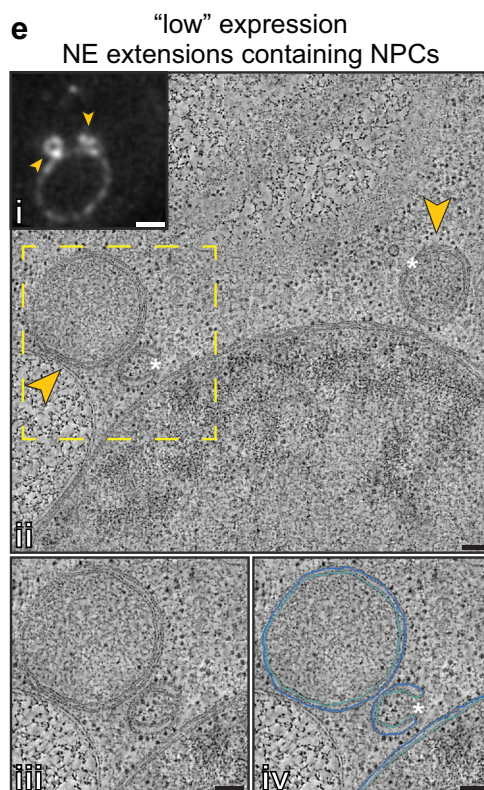
c



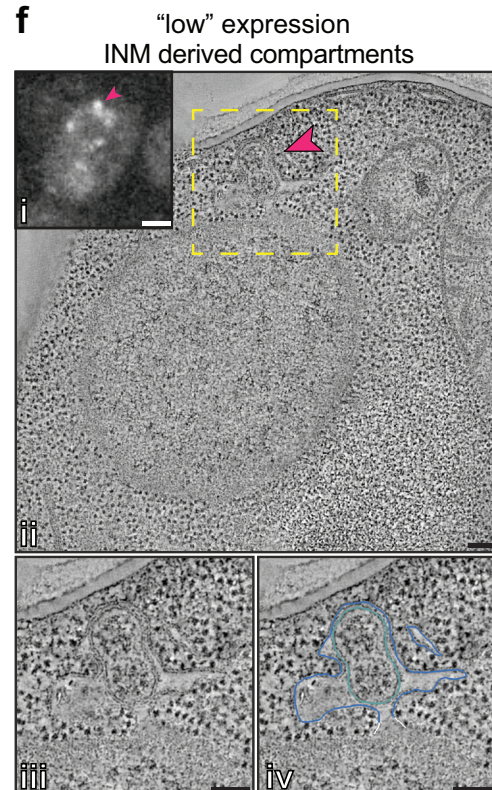
d



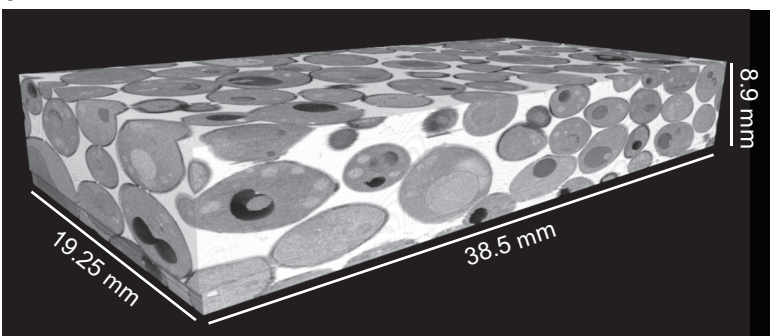
e



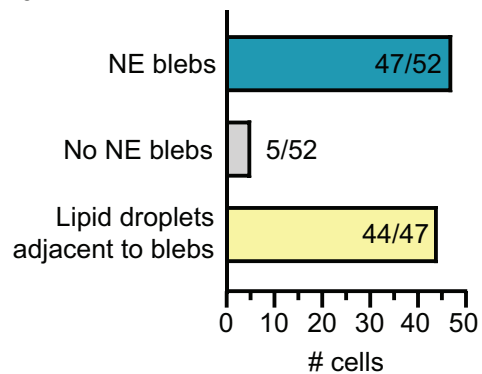
f



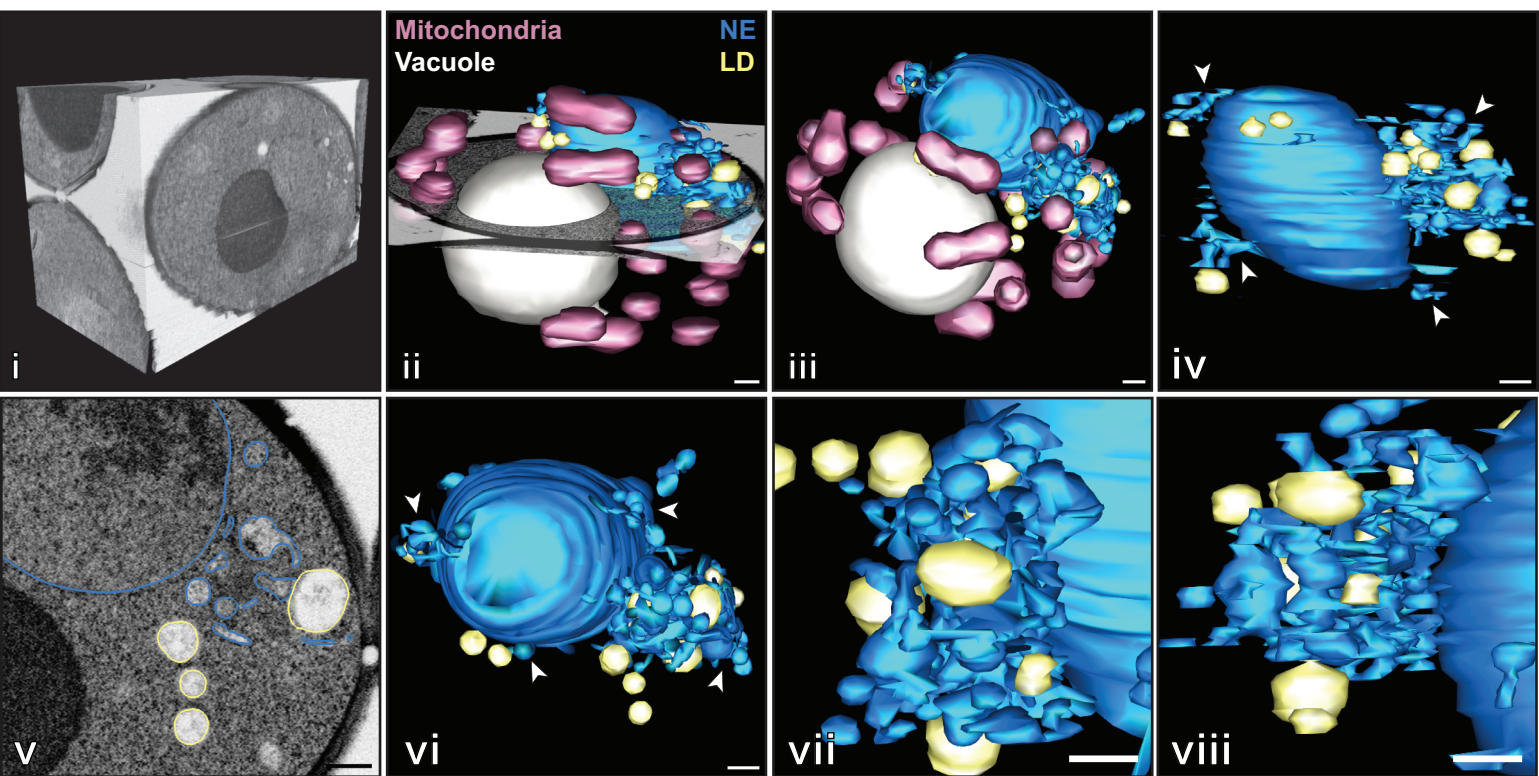
a



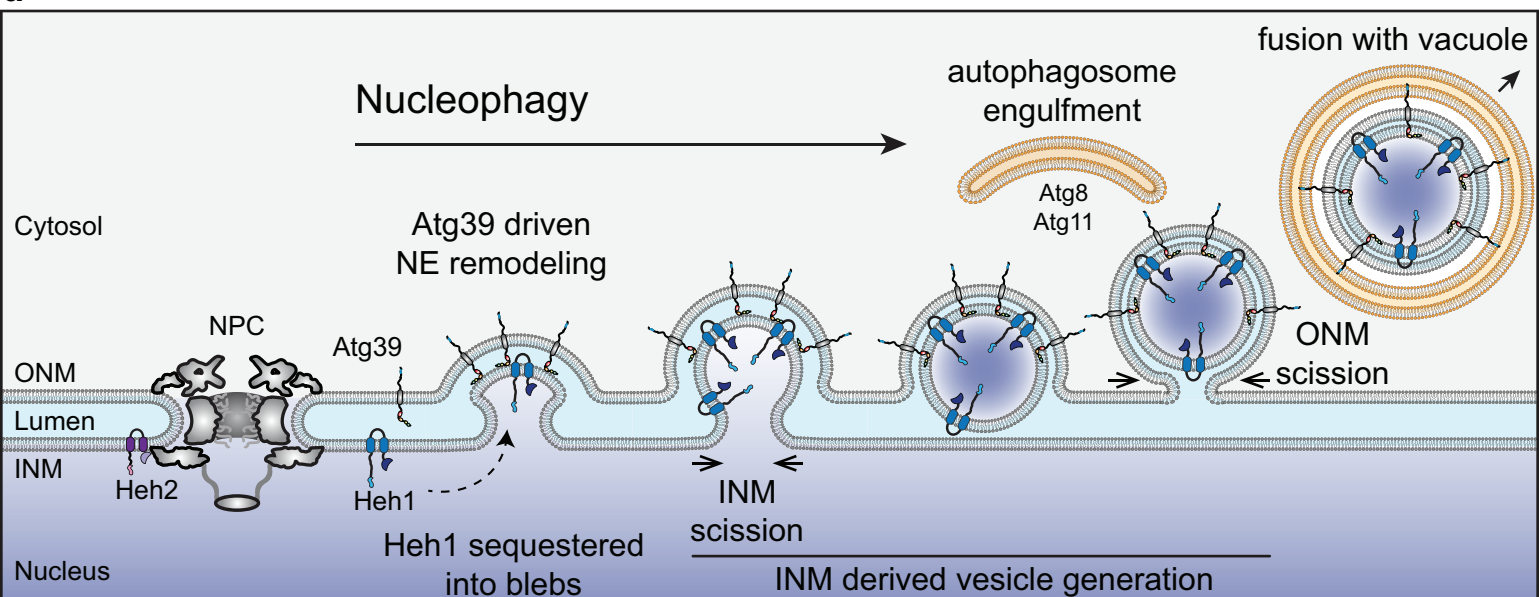
b



c



d



Supplementary Table 1: *S. cerevisiae* strains

Name	Genotype	Origin	Generation
W303a	<i>MATa, ade2-1 can1-100 his3-11,15 leu2-3,112 trp1-1 ura3-1</i>	EUROSCARF	
W303α	<i>MATa, ade2-1 can1-100 his3-11,15 leu2-3,112 trp1-1 ura3-1</i>	EUROSCARF	
FIGURE 1			
PMCL21	W303, <i>natMX6::GAL1-ATG39-GFP¹⁻¹⁰::CaURA3MX</i>	This study	Transformation of DTCPL1589 with PCR product
PMCL34	W303, <i>kanMX6::GAL1-GFP¹⁻¹⁰-ATG39</i>	This study	Transformation of W303 with PCR product
PMCL35	W303, <i>kanMX6::GAL1-GFP¹⁻¹⁰-atg39-(139-398)</i>	This study	Transformation of W303 with PCR product
PMCL298	W303, <i>kanMX6::GAL1-GFP¹⁻¹⁰-atg39-(1-169)::hphMX6</i>	This study	Transformation of PMCL34 with PCR product
FIGURE 2			
PMCL87	W303, <i>kanMX6::GAL1-GFP-ATG39</i>	This study	Transformation of W303 with PCR product
PMCL112	W303, <i>kanMX6::GAL1-GFP-atg39-(1-169)::hphMX6</i>	This study	Transformation of PMCL87 with PCR product
PMCL113	W303, <i>kanMX6::GAL1-GFP-atg39-(1-275)::hphMX6</i>	This study	Transformation of PMCL87 with PCR product
PMCL114	W303, <i>kanMX6::GAL1-GFP-atg39-(1-312)::hphMX6</i>	This study	Transformation of PMCL87 with PCR product
PMCL115	W303, <i>kanMX6::GAL1-GFP-atg39-(1-333)::hphMX6</i>	This study	Transformation of PMCL87 with PCR product
PMCL29	W303, <i>kanMX6::GAL1-GFP-atg39-(139-398)</i>	This study	Transformation of W303 with PCR product
PMCL390	W303, <i>TRP1::GAL1-GFP-atg39-(70-398)</i>	This study	Transformation of W303 with PCR product
PMCL392	W303, <i>his3MX6::GAL1-GFP-atg39-(120-398)</i>	This study	Transformation of W303 with PCR product
PMCL422	W303, <i>kanMX6::GAL1-GFP-Atg39 atg8Δ::natMX6</i>	This study	Progeny from cross between PMCL86 and PMCL16
PMCL424	W303, <i>kanMX6::GAL1-GFP-Atg39 atg11Δ::hphMX6</i>	This study	Progeny from cross between BWCL1377 and PMCL87
PMCL471	W303, <i>kanMX6::GAL1-GFP-Atg39 atg8Δ::natMX6 atg11Δ::hphMX6</i>	This study	Progeny from cross between PMCL422 and BWCL1378
FIGURE 3			
SCCPL113	W303, <i>ADE2 HEH1-GFP::TRP1 ATG39-3xHA::his3MX6</i>	This study	Transformation of DTCPL1221 with PCR product
SCCPL115	W303, <i>ADE2 HEH1-GFP::TRP1 atg39-(1-169)::his3MX6</i>	This study	Transformation of DTCPL1221 with PCR product
PMCL410	W303, <i>HEH1-GFP::TRP1 atg39-(1-333)::his3MX6</i>	This study	Progeny from cross between DTCPL999 and PMCL195
PMCL411	W303, <i>HEH1-GFP::TRP1 atg39-(1-312)::his3MX6</i>	This study	Progeny from cross between DTCPL999 and PMCL196
PMCL412	W303, <i>HEH1-GFP::TRP1 atg39-(1-275)::his3MX6</i>	This study	Progeny from cross between DTCPL999 and PMCL197
PMCL438	W303, <i>HEH1-GFP::TRP1 atg39Δ::hphMX6</i>	This study	Progeny from cross between DTCPL1215 and PMCL304
SCCPL114	W303, <i>ADE2 HEH2-GFP::TRP1 ATG39-3xHA::his3MX6</i>	This study	Transformation of DTCPL1219 with PCR product
SCCPL116	W303, <i>ADE2 HEH2-GFP::TRP1 atg39-(1-169)-3xHA::his3MX6</i>	This study	Transformation of DTCPL1219 with PCR product
PMCL374	W303, <i>ADE2 HEH2-GFP::TRP1 atg39Δ::natMX6</i>	This study	Progeny from cross between DTCPL1219 and PMCL359
PMCL377	W303, <i>ADE2 NUP82-GFP::TRP1 ATG39-3xHA::his3MX6</i>	This study	Transformation of PMCL371 with PCR product
PMCL378	W303, <i>ADE2 NUP2-GFP::TRP1 atg39-(1-169)-3xHA::his3MX6</i>	This study	Transformation of PMCL371 with PCR product
PMCL372	W303, <i>ADE2 NUP82-GFP::TRP1 atg39Δ::natMX6</i>	This study	Progeny from cross between SBCPL74 and PMCL359
SCCPL22	W303, <i>his3MX6::GAL1-ATG39-GFP::TRP1 pep4Δ::hphMX6</i>	This study	Progeny from cross between DTCPL688 and BWCL1374
FIGURE 4			
SCCPL39	W303, <i>ADE2 TRP1::GAL1-3xHA-mCherry-ATG39 HEH1-GFP::natMX6</i>	This study	Progeny from cross between SCCPL33 and CPL781
SCCPL95	W303, <i>ADE2 kanMX6::GAL1-mCherry-ATG39 heh1Δ::natMX6 pRS405-GFP-heh1-(1-443)-HindIII-heh1-(449-477)::LEU2</i>	This study	Transformation of linearized pSC8 into SCCPL44
SCCPL131	W303, <i>ADE2 kanMX6::GAL1-mCherry-ATG39 NUP85-GFP::his3MX6</i>	This study	Progeny from cross between SCCPL35 and SBCPL116
DTCPL911	W303, <i>his3MX6::GAL1-ATG39-GFP::TRP1 SPC42-mCherry::natMX6</i>	This study	Progeny from cross between DTCPL689 and MCCPL25
SCCPL40	W303, <i>ADE2 TRP1::GAL1-mCherry-3xHA-ATG39 HEH2-GFP::natMX6</i>	This study	Progeny from cross between SCCPL33 and CPL782
SCCPL80	W303, <i>ADE2 kanMX6::GAL1-mCherry-3xHA-ATG39 heh2-(1-570)-GFP::his3MX6</i>	This study	Progeny from cross between SCCPL35 and SBCPL40
FIGURE 5			
PMCL87	W303, <i>kanMX6::GAL1-GFP-ATG39</i>	This study	Transformation of W303 with PCR product
DTCPL688	W303, <i>his3MX6::GAL1-ATG39-GFP::TRP1</i>	This study	Transformation of DTMB05 with PCR product
FIGURE S1			
PMCL34	W303, <i>kanMX6::GAL1-GFP¹⁻¹⁰-ATG39</i>	This study	Transformation of W303 with PCR product
PMCL35	W303, <i>kanMX6::GAL1-GFP¹⁻¹⁰-atg39-(139-398)</i>	This study	Transformation of W303 with PCR product

PMCPL298	W303, <i>kanMX6::GAL1-GFP¹⁻¹⁰-atg39-(1-169)::hphMX6</i>	This study	Transformation of PMCPL34 with PCR product
PMCPL29	W303, <i>kanMX6::GAL1-GFP-atg39-(139-398)</i>	This study	Transformation of W303 with PCR product
PMCPL28	W303, <i>kanMX6::GAL1-GFP-atg39-(144-398)</i>	This study	Transformation of W303 with PCR product

FIGURE S2

PMCPL87	W303, <i>kanMX6::GAL1-GFP-ATG39</i>	This study	Transformation of W303 with PCR product
PMCPL115	W303, <i>kanMX6::GAL1-GFP-atg39-(1-333)::hphMX6</i>	This study	Transformation of PMCPL87 with PCR product
PMCPL114	W303, <i>kanMX6::GAL1-GFP-atg39-(1-312)::hphMX6</i>	This study	Transformation of PMCPL87 with PCR product
PMCPL113	W303, <i>kanMX6::GAL1-GFP-atg39-(1-275)::hphMX6</i>	This study	Transformation of PMCPL87 with PCR product
PMCPL112	W303, <i>kanMX6::GAL1-GFP-atg39-(1-169)::hphMX6</i>	This study	Transformation of PMCPL87 with PCR product
PMCPL390	W303, <i>TRP1::GAL1-GFP-atg39-(70-398)</i>	This study	Transformation of W303 with PCR product
PMCPL392	W303, <i>his3MX6::GAL1-GFP-atg39-(120-398)</i>	This study	Transformation of W303 with PCR product
PMCPL29	W303, <i>kanMX6::GAL1-GFP-atg39-(139-398)</i>	This study	Transformation of W303 with PCR product
DTCP688	W303, <i>his3MX6::GAL1-ATG39-GFP::TRP1</i>	This study	Transformation of DTMB05 with PCR product
SCCPL22	W303, <i>his3MX6::GAL1-ATG39-GFP::TRP1 pep4Δ::hphMX6</i>	This study	Progeny from cross between DTCP688 and BWCPL1374
SCCPL01	W303, <i>hphMX6::GAL1-ATG39-GFP::TRP1</i>	This study	Transformation of DTCP688 with PCR product
SCCPL03	W303, <i>hphMX6::GAL1-atg39-(1-169)-GFP::TRP1</i>	This study	Transformation of DTCP980 with PCR product
PMCPL24	W303, <i>hphMX6::GAL1-ATG39-GFP::TRP1 atg8::natMX6</i>	This study	Progeny from cross between SCCPL01 and PMCPL15
PMCPL22	W303, <i>hphMX6::GAL1-ATG39-GFP::TRP1 atg11::hphMX6</i>	This study	Progeny from cross between SCCPL01 and PMCPL18
PMCPL23	W303, <i>hphMX6::GAL1-ATG39-GFP::TRP1 atg8::natMX6 atg11::hphMX6</i>	This study	Progeny from cross between SCCPL01 and PMCPL18
PMCPL422	W303, <i>kanMX6::GAL1-GFP-Atg39 atg8Δ::natMX6</i>	This study	Progeny from cross between PMCPL86 and PMCPL16
PMCPL424	W303, <i>kanMX6::GAL1-GFP-Atg39 atg11Δ::hphMX6</i>	This study	Progeny from cross between BWCPL1377 and PMCPL87
PMCPL471	W303, <i>kanMX6::GAL1-GFP-Atg39 atg8Δ::natMX6 atg11Δ::hphMX6</i>	This study	Progeny from cross between PMCPL422 and BWCPL1378

FIGURE S3

PMCPL25	W303, <i>his3MX6::GAL1-ATG39-mCherry::kanMX6 heh1-(1-479)-GFP::TRP1</i>	This study	Progeny from cross between DTCP942 and PMCPL04
---------	---	------------	--

FIGURE S4

SCCPL35	W303, <i>kanMX6::GAL1-mCherry-ATG39</i>	This study	Transformation of W303 with PCR product
PMCPL87	W303, <i>kanMX6::GAL1-GFP-ATG39</i>	This study	Transformation of W303 with PCR product
DTCP688	W303, <i>his3MX6::GAL1-ATG39-GFP::TRP1</i>	This study	Transformation of DTMB05 with PCR product

FIGURE S5

DTCP688	W303, <i>his3MX6::GAL1-ATG39-GFP::TRP1</i>	This study	Transformation of DTMB05 with PCR product
---------	--	------------	---

Supplementary Table 2: Plasmids used in this study.

Name	Description	Origin
pFA6a-his3MX6-GAL1	Template for PCR based chromosomal integration of GAL1 promoter	⁷⁴
pFA6a-kanMX6-GAL1	Template for PCR based chromosomal integration of GAL1 promoter	⁷⁴
pFA6a-TRP1-GAL1	Template for PCR based chromosomal integration of GAL1 promoter	⁷⁴
pFA6a-kanMX6-GAL1-mCherry	Template for PCR based chromosomal integration of GAL1 promoter and mCherry ORF	This study
pFA6a-TRP1-GAL1-mCherry-3xHA	Template for PCR based chromosomal integration of GAL1 promoter and mCherry-3xHA ORF	This study
pFA6a-GFP-hisMX6	Template for PCR based chromosomal integration of GFP ORF	⁷⁴
pFA6a-GFP-TRP1	Template for PCR based chromosomal integration of GFP ORF	⁷⁴
pFA6a-GFP-natMX6	Template for PCR based chromosomal integration of GFP ORF	⁷⁵
pFA6a-mCherry-natMX6	Template for PCR based chromosomal integration of mCherry ORF	EUROSCARF
pFA6a-his3MX6	Template for PCR based chromosomal integration of his3MX6 cassette	⁷⁴
pFA6a-hphMX6	Template for PCR based chromosomal integration of hphMX6 cassette	⁷⁴
pFA6a-natMX6	Template for PCR based chromosomal integration of natMX6 cassette	⁷⁵
pFA6a-3xHA-mCherry-natMX6	Template for PCR based chromosomal integration of 3xHA-mCherry ORF	This study
pFA6a-3xHA-hisMX6	Template for PCR based chromosomal integration of 3xHA	⁷⁴
pRS405	YIP- <i>LEU2</i>	ATCC
pRS415	<i>CEN6, LEU2</i>	ATCC
pSC8	pRS405-GFP-heh1-(1-443)-HindIII-heh1-(449-477):: <i>LEU2</i>	This study
pPM1	pFA6a-kanMX6-GAL1-GFP ¹⁻¹⁰	This study
pSJ1602	pRS315-NOP1pr-mCherry-SCS2TM-GFP ¹¹	Gift from Sue Jaspersen, Addgene plasmid # 86417 ; http://n2t.net/addgene:86417 ; RRID:Addgene_86417
pSJ1321	pRS315-NOP1pr-GFP ¹¹ -mCherry-PUS1	Gift from Sue Jaspersen, Addgene plasmid # 86413 ; http://n2t.net/addgene:86413 ; RRID:Addgene_86413
pSJ1568	pRS315-NOP1pr-GFP ¹¹ -mCherry-SCS2TM	Gift from Sue Jaspersen, Addgene plasmid # 86416 ; http://n2t.net/addgene:86416 ; RRID:Addgene_86416
pSJ1256	pFA6a-link-yGFP ¹⁻¹⁰ -CaURA3MX	Gift from Sue Jaspersen, Addgene plasmid # 86419 ; http://n2t.net/addgene:86419 ; RRID:Addgene_86419